

高次元形態情報に基づく多面的定量的フェノタイピング：

カルシウム制御経路の解析とマイクロ流体技術を使用する

ハイスループット顕微鏡撮影システムの試験的導入

東京大学大学院
新領域創成科学研究科
先端生命科学専攻

大貫 慎輔

2007 年

修士論文

**Multilateral quantitative phenotyping based on high-dimensional
morphological data:**

**Analysis of Ca^{2+} -regulatory pathways and feasibility study of high-throughput
microphotography system using microfluidics**

Department of Integrated Biosciences
Graduate School of Frontier Sciences
University of Tokyo

Shinsuke Ohnuki

2007

Master Thesis

TABLE OF CONTENTS

Acknowledgements	5
List of Tables	6
List of Figures	7
Abbreviations	8
Abstract	9
General introduction	10
Chapter 1: Multiple Ca^{2+}-regulatory pathways revealed by morphological phenotyping of Ca^{2+}-sensitive mutants of <i>Saccharomyces cerevisiae</i>	
Introduction	12
Material and Methods	14
Results	18
Discussion	24
Figure Legends	31
Table 1-2	36
Figures 1-9	46
Chapter 2: Feasibility study of high-throughput microphotography system using microfluidics	
Introduction	61
Materials and Methods	64
Results	66

Discussion	69
Figure Legends	71
Table 3-4	72
Figures 8-10	75
References	78
Publications	83

ACKNOWLEDGMENTS

I would like to express my deepest gratitude to Professor Yoshikazu Ohya for his constant supervision, guidance, advice and cheerful encouragement throughout this study.

I would like to express my deep appreciation to Associate Professor Kintake Sonoike for his advice and encouragement throughout this study.

I would like to express my appreciation to Professor Shinichi Morishita for his work and manuscript reading.

I would like to express my appreciation to Associate Professor Dai hirata for his manuscript reading and advice.

I am deeply grateful to Dr. Satoru Nogami for his constant guidance, advice, suggestion and encouragement throughout this study.

I am grateful to Yoichiro Nakatani for his manuscript reading and statistical advice throughout my study.

I wish to thank Mizuho Sekiya, Machika Watanabe and Takahiro Negishi for their kind advice and encouragement.

I would like to thank Tamao Goto and Yuka Kitamura for technical assistance.

I would like to thank all the members of Laboratory of Signal Transduction, Department of Integrated Biosciences, Graduate School of Frontier Sciences, University of Tokyo, for their warm encouragement and support throughout my study.

Last but not least, I would like to thank my parents for understanding towards my study.

LIST OF TABLES

Table 1. List of yeast strains used in this study

Table 2. The significantly changed parameters of wild-type under containing high-concentration of Ca^{2+} .

Table 3. Measurements of fabricated microchannels.

Table4. Morphological parameter values of yeast cells under each condition.

LIST OF FIGURES

Figure 1. The 59 mean parameters showing differences between the effects of high and low concentrations of Ca^{2+} on wild-type yeast cells.

Figure 2. Illustration of morphological changes induced by extracellular Ca^{2+} in wild-type cells. The $+\text{Ca}^{2+}$ and $-\text{Ca}^{2+}$ designations indicate high and low concentrations of Ca^{2+} in the medium, respectively.

Figure 3. Number of significantly changed parameters in calcium-sensitive yeast strains.

Figure 4. Cluster analysis of the *c/s* mutants based on the similarities of the morphological changes.

Figure 5. Clustering of randomized data.

Figure 6. Cluster dendrogram of the *c/s* mutants based on the similarities of the morphological changes using averaged data.

Figure 7. Coherently changed parameters in each class.

Figure 8. Characteristic morphological changes in each class. **a-g** represent lists of parameters that show characteristic changes in class I-VII, respectively.

Figure 9. 2D plots of coherently changed parameters in each class.

Figure 10. The microfluidic chip used in this study.

Figure 11. Phase-contrast images of microchannels.

Figure 12. Microphotographs of yeast cells for image analysis using CalMorph.

ABBREVIATIONS

cls	: calcium-sensitive
<i>MAT</i>	: mating type
vma	: vacuolar-membrane ATPase
vps	: vacuolar protein sorting
YPD	: Yeast extract polypeptone dextrose medium
WT	: wild-type
WT+Ca ²⁺	: wild-type cells in a high concentration of Ca ²⁺
WT-Ca ²⁺	: wild-type cells in a low concentration of Ca ²⁺
PDMS	: polydimethylsiloxane

ABSTRACT

Multilateral and quantitative phenotypic analysis based on high-dimensional morphological data is a powerful tool for understanding intracellular genetic network. Yeast cell morphology can be treated as a quantitative trait using the image processing software CalMorph. Here, I investigated Ca^{2+} -induced morphological changes in Ca^{2+} -sensitive (*c/s*) mutants of *Saccharomyces cerevisiae*, inspired by the discovery that the characteristic Ca^{2+} -induced morphological changes in the Ca^{2+} -sensitive mutant *zds1* reflect disorder in the Ca^{2+} signaling-mediated cell-cycle control pathway. I developed a novel method for high-dimensional and quantitative phenotypic analysis which demonstrates that 31 of 58 *c/s* mutants were classified into seven classes, and the patterns of morphological change induced by Ca^{2+} in one class differed from those of another class. I conclude that a high concentration of Ca^{2+} exerts a wide variety of effects on yeast and that there are multiple Ca^{2+} -regulatory pathways that are distinct from the Zds1p-related pathway. To improve the throughput of microphotography, I designed microchannels using microfluidics technology. Yeast cell images under high-magnification microscopy were successfully obtained using the designed microchannels, suggesting that the high-throughput microphotography system can be developed using this technology.

GENERAL INTRODUCTION

Phenotypic analysis of the mutants has been a useful approach to understand intracellular genetic network because phenotypes including auxotrophy, drug resistance, and cellular morphology is tightly linked to cellular processes and functions in virtually all eukaryotic organisms. In *Saccharomyces cerevisiae*, it was revealed that the Ca^{2+} signaling mediates the cell cycle progression by analyzing a *zds1* mutant which shows unique morphological changes by adding high concentration of Ca^{2+} into medium (Mizunuma et al., 1998). Recently, a novel strategy for understanding genomic functions was proposed according to findings that the cell morphology and gene functions were tightly related based on quantitative morphological data from all of nonessential gene deletion mutants in *Saccharomyces cerevisiae* (Ohya et al., 2005). Hence, I propose that the analysis of phenotypes that reflect responses to extracellular multilateral environment of all mutants must be a powerful approach to reveal whole of genetic network which is one of the goal in cellular signal transduction study. To proceed the study in this line, following two problems need to be solved. First, methods for high-dimensional and quantitative phenotypic analysis has not established yet. Second, there is no high-throughput experimental system which enables to obtain multilateral, high-dimensional and quantitative morphological data from all of mutants.

In this thesis, I attempted to solve these two problems. First, to develop and demonstrate the methods for high-dimensional and quantitative phenotypic analysis, I thoroughly analyzed the calcium-induced morphological changes of *zds1* mutant and 58 *cls* mutants which were screened in

our laboratory (chapter I). Second, I tried developing the high-throughput microphotography system which is enabling to scale-down and speed-up the microphotograph acquisition (chapter II).

CHAPTER 1

Diversity of Ca^{2+} -induced morphology revealed by morphological phenotyping of Ca^{2+} -sensitive mutants of *Saccharomyces cerevisiae*

INTRODUCTION

Cellular morphology is tightly linked to cellular processes and functions in virtually all eukaryotic organisms. In the yeast *Saccharomyces cerevisiae*, the elliptical shape sequentially changes with cell-cycle progression under nutritionally rich conditions (Hartwell, 1991; Pruyne and Bretscher, 2000). Under particular conditions, yeast cells drastically change their morphology, forming the shmoo tip (pear-like cell morphology) under mating conditions (Trueheart et al., 1987), and pseudohyphae (filamentous cell morphology) or ascospores (four cells within a cell) under starvation conditions (Lynn and Magee, 1970; Mosch and Fink, 1997).

Since cell morphology changes during the yeast cell cycle, drastic morphological changes can be induced in yeast cells by adding reagents that inhibit cell-cycle progression. Large budded cells accumulate following treatment with hydroxyurea (Lord and Wheals, 1983), which inhibits ribonucleotide reductase. Treatment of *zds1* (zillion different screens (Bi and Pringle, 1996; Yu et al., 1996)) mutant cells with 50-300 mM of Ca^{2+} induces G2/M arrest and the formation of elongated buds with one nucleus at the mother/bud, which indicates that the Ca^{2+} -signaling pathway mediates cell cycle control via repression of the *SWE1* transcription in G2 phase (Mizunuma et al., 1998). Genes that are involved in the *Zds1*-mediated Ca^{2+} signaling pathway have been identified

(Mizunuma et al., 2004; Yokoyama et al., 2006). However, *Zds1*-dependent, Ca^{2+} -mediated, cell cycle control may be only a part of the Ca^{2+} -signaling pathway, since many Ca^{2+} -sensitive (*cls*) mutants have been reported (Cunningham and Fink, 1994; Kucharczyk et al., 2001; Ohya et al., 1986b). Ohya *et al.* identified 18 complementation groups (unsaturated) of *cls* mutants (Ohya et al., 1986b), some of which have been implicated in intracellular Ca^{2+} homeostasis (Hirata et al., 1993; Ohya et al., 1991). It remains unknown whether the morphological features and cellular functions of these *cls* mutants are similar to those of the *zds1* mutant.

In the present study, I analyzed 58 *cls* mutants for morphological changes induced by Ca^{2+} based on high-dimensional and quantitative morphological information obtained using the CalMorph program (Ohya et al., 2005). My statistical and multivariate analyses reveal that wild-type yeast cells undergo various types of morphological change in response to Ca^{2+} . Thirty one *cls* mutants were clustered into seven groups based on shared characteristic changes. This is the first demonstration that quantitative comprehensive phenotypic analyses of yeast mutants can be used to assess reagent-induced effects that cannot be discriminated in the wild-type strain.

MATERIALS AND METHODS

Media and Strains

The strains used in this work are listed in Table 1. The strains bearing single gene deletion by a *KanMX4* cassette were purchased from the EUROSCARF collection (available on the World Wide Web at www.uni-frankfurt.de/fb15/mikro/euroscarf/2000). The medium for growing *S. cerevisiae* was YPD that contained 1% (w/v) Bacto-yeast extract (BD Biosciences), 2% (w/v) polypeptone (WAKO), and 2% (w/v) dextrose. YPD pH 5.5 medium was YPD medium that was buffered to pH 5.5 with 50 mM succinate/NaOH. For examination of Ca^{2+} sensitivity, YPD supplemented with 100 mM CaCl_2 was used as a Ca^{2+} -rich medium. Solid media were prepared by adding 2% (w/v) agar to the above media.

Fluorescence Staining and Microscopy

Cells (8×10^6 cells) at log-phase in YPD were collected, washed once in YPD with or without 100 mM CaCl_2 , and resuspended in 4 ml of the respective medium to a final concentration of $2 \times 10^6/\text{ml}$. The cells were incubated for 5 h at 30°C, washed once with YPD, and fixed in YPD that was supplemented with 3.7% formaldehyde and 0.1 M potassium phosphate buffer (pH 6.5). Triple-staining of the yeast cells and image analysis with CalMorph were performed as described previously (Ohya et al., 2005). CalMorph automatically characterizes each yeast cell using 501 morphological parameters. Ten and five independent cultures grown under the two different conditions were analyzed for the wild-type and mutant cells, respectively.

Assessment of Parameters Changed by Ca²⁺ Treatment

All the statistical analyses were performed using R (<http://www.r-project.org/>). To investigate the Ca²⁺ effect on yeast cell morphology, I tested the difference between the ten high Ca²⁺ and ten low Ca²⁺ values using the U test for each parameter (Mann and Whitney, 1947). The number of parameters expected to be detected by chance was estimated by empirical permutation tests (Churchill and Doerge, 1994).

Data Preprocessing

To generate uniform distributions of each parameter value, I transformed the parameter values to statistic U (Mann and Whitney, 1947) and modified them to reflect the direction of morphological change. The samples and controls were combined and ranked in order of the lowest values first. Note that the same values were ranked in average order. Then, I summed the rank order of samples to T and computed U' , which is a modified statistic U value defined by the function:

$$U' = T - \frac{m(m+n+1)}{2}$$

where m and n are the sample sizes of the test samples and controls, respectively. The probability distribution of U' is the same as the Mann-Whitney statistic U . However, the larger the sample value, the larger the value of U' becomes; U' was set to 0 when the distribution of the samples was equal to that of the controls.

Hierarchical Clustering

Hierarchical clustering was performed using R (<http://www.r-project.org/>). TreeView ver. 1.60 was used to visualize the clustering results (Eisen et al., 1998). Clusters were assessed using the R package pvclust tool (<http://www.is.titech.ac.jp/~shimo/prog/pvclust/>) at $P > 0.95$ (Suzuki and Shimodaira, 2006). The options used in pvclust were: method.hclust = "average"; nboot = 1000; r = seq(0.5, 1.4, by = 0.1). For dissimilarity, see the *Metrics* section below.

Metrics

The morphological dissimilarity metric that I used is a form of angle. Let the morphological vector \vec{m} equal an ordered set of U' for the mutants. For any two mutants $\vec{a} \in \vec{m}$ and $\vec{b} \in \vec{m}$, the morphological dissimilarity score can be computed as follows:

$$S(\vec{a}, \vec{b}) = \arccos\left(\frac{\vec{a} \cdot \vec{b}}{|\vec{a}| |\vec{b}|}\right) \times \frac{360}{2\pi}$$

The parameter dissimilarity metric that I used is a form of Spearman's rank correlation coefficient.

Let P_i equal the rank order of the primary data for parameter P in independent culture i . For any two parameters $X \in P$ and $Y \in P$ observed over a series of N cultures combined under both conditions, the parameter dissimilarity score can be computed as follows:

$$S(X, Y) = 1 - |R(X, Y)|$$

where

$$R(X, Y) = 1 - \frac{6}{N(N+1)(N-1)} \sum_{i=1}^N (X_i - Y_i)^2.$$

Detection of Parameters Coherently Changed in Each Class

Based on the assumption that a characteristic parameter of an identified class is a similarly changed parameter among the mutants, I defined the statistic U_c' , which represents the coherency in the change of direction of the parameter as $U_c' = U_1' + U_2' + \dots + U_l'$, where l is the number of mutants included in the class, U_l' is statistic U' of the l th mutant, and U' is as defined in the *Data Preprocessing* section. To estimate the critical value of U_c' that served as a certain threshold value, I computed the population distribution of U_c' for each value of l . The total number of combinations for U_c' is defined by $((m+n)C_n)^l$, since the number of combinations for U' is calculated as $(m+n)C_n$, where m and n are the sizes of the control data and sample data, respectively. Then, the p -values that correspond to each U_c' are calculated based on the distribution of the $((m+n)C_n)^l$ values. Given a threshold value, a parameter is judged to be a coherently changed parameter if the absolute value of U_c' is higher than the critical value, which gives the threshold value of the two-sided p -value.

RESULTS

Changes in Yeast Morphology Caused by a High Concentration of Extracellular Ca^{2+}

To investigate the effect of extracellular Ca^{2+} concentration on wild-type yeast morphology, I compared the cellular morphologies of wild-type yeasts grown under two culture conditions (low and high concentrations of Ca^{2+}). For simplicity, wild-type cells treated with low and high concentrations of Ca^{2+} are referred to as WT- Ca^{2+} and WT+ Ca^{2+} , respectively. Samples from ten independent cultures under each condition were characterized by triple-staining fluorescence microscopy and automated cell imaging, as described previously (Ohya et al., 2005). At least 200 cells were analyzed per culture to quantify 501 morphological parameters. For each parameter, I tested the difference between the ten WT- Ca^{2+} and the ten WT+ Ca^{2+} values using the Mann-Whitney test (Mann and Whitney, 1947). Table 1 shows the significant morphological differences that were noted between the ten WT- Ca^{2+} and the ten WT+ Ca^{2+} values in 100, 65, and 38 parameters at $P < 0.05$, $P < 0.01$, and $P < 0.001$, respectively. A permutation test shows that twenty of the hundred parameters were expected to be detected by chance at $P < 0.05$. At $P < 0.001$, fewer than one of the 38 parameters is expected to be detected by chance (see *Materials and Methods* section).

I also investigated the profiles of the Ca^{2+} -dependent morphological changes. Among the 100 parameters detected, I focused on 59 parameters that represented a mean of the measured cells, since the remainder of the parameters represented coefficients of variations in the measurements. When I applied average-linkage hierarchical clustering with dissimilarity based on the Spearman

rank order correlation coefficient, I found tightly clustered parameters (Figure 1). According to these classified parameters, I illustrate the Ca^{2+} -dependent morphological changes based on the features reflected in two or more parameters (Figure 2). In addition to the global changes observed in all cell-cycle stages, stage-specific changes were observed. In the WT+ Ca^{2+} condition, rounded cells with centered nuclei accumulated in all stages. In addition, cells with round nuclei accumulated in the unbudded stage, cells with a straightened budding site and direction with a wide neck and large actin region accumulated in all budded stages, and cells with proximity of the actin patch to the neck accumulated in the stage of budded cells with two nuclei (Figure 2). These results clearly indicate that the morphological differences between WT- Ca^{2+} and WT+ Ca^{2+} cells occur at different stages of the cell cycle and reflect various cellular aspects.

Morphological Changes in *cls* Mutants Induced by a High Concentration of Extracellular Ca^{2+}

It has been reported that several yeast mutants change morphology under conditions of high Ca^{2+} . For example, a calcium-sensitive *cls4* mutant of *S. cerevisiae* stops dividing in the presence of 100 mM Ca^{2+} , producing large, rounded, and unbudded cells (Ohya et al., 1986a). In addition, the *zds1* mutant shows defective growth in rich medium in the presence of 50-300 mM Ca^{2+} , with the cells forming an elongated bud and most of the elongated cells having a single nucleus at the mother/bud neck, which is characteristic of G2 delay (Mizunuma et al., 1998). Therefore, I expected that some of the *cls* mutants would change their morphology in the presence of a high concentration of Ca^{2+} . I analyzed the morphological changes of 60 strains, including the wild-type and *zds1* mutant, in

addition to the 58 *cls* mutants from five independent cultures under conditions of low and high concentrations of Ca^{2+} in the medium. I used the Mann-Whitney test (Mann and Whitney, 1947) at $P < 0.01$ to detect differences between the two conditions for each parameter and counted the number of parameters significantly changed in each mutant (Figure 3). The morphological changes of *zds1* mutant cells were observed in 13 parameters (Figure 3). Among them, C114_C (bud axis ratio of budded cell with two nuclei) gave most significant increase. In addition to confirmation of Ca^{2+} -induced elongated bud morphology in the *zds1* mutant, I describe other 12 phenotypes associated with the *zds1* mutant in the presence of high concentration of Ca^{2+} (Figure 3). The number of significantly changed parameters detected in at least one strain was 278 out of 501, whereas 128 of these would be expected to be detected by chance (see *Materials and Methods* section). Since the wild-type showed morphological changes in 11 parameters (Figure 3), fewer than 3 of which would be expected to be detected by chance, the number of significantly changed parameters in the *cls* mutants was ten-fold higher than that detected in the wild-type strain. This suggests that the intensity and diversity of the effect of extracellular Ca^{2+} on morphological change vary for each strain.

The *cls* mutants can be functionally classified based on the similarities of morphological changes induced by Ca^{2+} , since my quantitative morphological analysis of yeast deletion mutants reveals that similar morphological changes are induced when similar intracellular functions are affected (Ohya et al., 2005). In order to represent the similarities of the morphological changes between mutants, the modified *U* statistic was used in the data processing (see *Materials and*

Methods section). I applied hierarchical clustering analysis to the morphological vectors of *cls* mutants using the positive angles between two arbitrary vectors as the dissimilarity (Figure 4). The red and green boxes in Figure 4 indicate increase and decrease of parameter values by Ca^{2+} treatment, respectively. Several mutants showed similar color patterns, suggesting that they share similar Ca^{2+} -induced morphological changes. On the other hand, different color patterns are shown in other strains, suggesting that there is a wide variety of the response pattern in the *cls* mutants.

To verify that the structure in Figure 4 is of biological origin and is not an artifact of the clustering procedure, the initial data from the yeast morphological response experiment transformed into the modified *U* statistic were randomized in three different ways and were clustered using the same procedure (Figure 5) (Eisen et al., 1998). No similar structure resulted from any of these randomized data sets, indicating that the patterns seen in Figures 4 depict a biological order in the environmental responses of the strains. Subsequently, to detect robustly clustered strains, I applied the multi-scale bootstrap technique (Suzuki and Shimodaira, 2006). At $P > 0.95$, I detected seven classes for a total of 32 strains at $P > 0.95$ (Figure 4). Of the seven classes, three (Classes III, VI, and VII) included mutants that are already known to be functionally related. On the other hand, when I employed the log-transformed average method (which is the standard preprocessing step) instead of the modified *U* statistic, fewer classes consisting of fewer mutants were detected (Figure 6). In addition, *VMA* mutants were divided into at least two classes. These results indicate that the modified *U* statistic is effective in identifying the class that is consistent with the functionally related mutants.

In order to understand the properties of each class of mutant, the characteristic common morphological changes of each class should be described. I detected the parameters whose values were coherently changed in the same direction in each class at $P < 0.01$ and summarized in Figure 7 (see *Materials and Methods* section). The red and green boxes in each class indicate parameters where values were significantly and coherently increased and decreased by Ca^{2+} -treatment, respectively. Pattern of the colored boxes were different among classes, suggesting that pattern of morphological changes common in each class are unique to the class (Figure 7). When the parameters that represented the coefficient of variance were discarded from all the detected parameters, the numbers of parameters were 37, 105, 28, 28, 28, 64, and 126 in Classes I to VII, respectively. As examples, Class I mutants contained a large nucleus and showed accumulation of small buds during growth in the Ca^{2+} -rich medium (Figure 8a). When modified U values of D174_C (maximal distance between nuclear gravity center and nuclear outline in bud) and C123 (small bud ratio to budded cells) are displayed on a two-dimensional scatter-plot, Class I mutant is plotted near to each other and is coherently far from coordinate origin (Figure 9A). Similarly, the cell sizes of Class III mutants were considered small because the long-axis lengths of the whole cells were short and cell roundness was increased (Figure 9B and 8c), in contrast to the large cell sizes of mutants of Classes II, VI, and VII (Figure 9C, 8b, 8f and 8g). In Classes II, VI, and VII, actin delocalization was also observed (Figure 9C, 8b, 8f and 8g). As shown in Figure 9D, bud axis ratio of budded cell gave most significant increase in the *zds1* mutant. These results suggest that the morphological changes induced by Ca^{2+} differ among classes, and that mutants that do not

belong to any class show different morphologies from those of all the other mutants. Therefore, I conclude that *c/s* mutants show various morphological changes when grown in a high concentration of Ca^{2+} .

DISCUSSION

With regard to the high-dimensional and quantitative phenotypic traits, I show that a high concentration of extracellular Ca^{2+} induces a wider variety of morphological changes in *c/s* mutants.

The quantitative data such as morphological parameters include a dispersion which is variation of values caused by experimental errors. This phenotypic study means that I can reflect not only the central value (e.g. mean and median) but also the dispersion (e.g. standard deviation and quartile deviation) to the high-dimensional cluster analysis using the data obtained from replicated experiments. Qualitative or categorical phenotypes have been used for classification of mutants without consideration of the dispersion of the data. Recently, in a gene expression profiling study, classes that consisted of genes with similar expression patterns were estimated by probability (Brown et al., 2006; Suzuki and Shimodaira, 2006). In the present study, more accurate and detailed phenotypic analyses were performed to identify classes of mutants with similar phenotypes based on probability. The method that I used is applicable to any quantitative phenotype (even a categorical phenotype) that is obtained from replicated experiments. Therefore, this method represents a powerful method for large-scale phenotypic analysis.

Identification of Phenotypically Similar Classes

Replication of the experiment is important when phenotypes obtained from CalMorph are used for phenotypic analysis. Phenotypic analysis using CalMorph was previously performed by Ohya and coworkers (Ohya et al., 2005). However, they analyzed the data obtained from a single experiment,

which was not replicated. Therefore the data included experimental errors; this makes it difficult to perform detailed analyses, such as the identification of mutants that have similar phenotypes. Using the data set obtained from replicated experiments using the 58 *c/s* mutants, I detected and characterized classes of mutants that showed similar phenotypes at $P > 0.95$, and I detected coherently changed parameters in each class at $P < 0.01$.

The modified test statistic derived from transformation of the data from the replicated experiments enabled us to use parameters with values that showed different distributions for the clustering, and to summarize the morphological similarities. Initially, I calculated the U statistic obtained from replicated experiments under the two conditions. Then, the U statistic was modified to reflect the direction of change and applied to the cluster analysis. Since the calculation process is based on the rank-order method, all of the parameter values were transformed to the same distribution irrespective of their original distributions. Therefore, this preprocessing method is applicable to any quantitative phenotypes that show different distributions.

Better clustering results can be obtained using the modified U statistic rather than the log-transformed average. In the analysis of expression data from microarrays, the standard preprocessing involves log-transformation of the expression values, i.e., the Cy5/Cy3 fluorescence ratios (Eisen et al., 1998), and the expression values are averaged (Kohane et al., 2003). When the morphological data were applied to the cluster analysis after this standard preprocessing step, few classes that contained functionally related mutants were identified (Figure 6). On the other hand, when the cluster analysis was performed after preprocessing with the modified U statistic, several

classes of functionally related mutants, such as iron ion transporter (Class III), Class C VPS (Class VI), and VMA (Class VII), were identified (Figure 4). These results suggest that the modified U statistic is effective in the classification of functionally related mutants.

Cluster Analysis Application

Having classified and characterized the *c/s* mutants based on morphological changes, I considered five potential problems: 1) the sample size for the clustering; 2) lack of unity in the data types of the parameters; 3) the selection of a dissimilarity metric; 4) validation of the clustering results; and 5) extraction of characteristic phenotypes. First, it is known that a clustering produced with a sample size of less than 50 (which is typical of a microarray study) is generally not reproducible (Garge et al., 2005). In the present study, I used 60 samples in the clustering of the mutants.

Second, the data type is restricted to only one type when the cluster analysis is applied (Kohane et al., 2003), although the parameter outputs from CalMorph have data types of length, number of cell, coefficient of variation etc. To overcome this problem, I made the data type uniform by transforming the parameter values to the modified U statistics.

Third, some dissimilarity metrics, such as Euclidean distance and the correlation coefficient, were expected to group several mutants as “weak-phenotype mutants”, since some mutants were weakly affected by Ca^{2+} (Figure 3). Therefore, I needed to extract the values that represented the nature of Ca^{2+} -induced morphological change from the morphological vectors of the mutants. The magnitude and direction of a morphological vector correspond to the affected intensity

and the nature of the morphological change, respectively (see *Materials and Methods* section). I accomplished the comparison of the nature of morphological change using angles as the dissimilarity.

Fourth, unsupervised classification of high-dimensional data should be validated using resampling-based procedures (Allison et al., 2006). The validation methods for the clustering results based on the resampling procedures have been reported in the methodology for microarray data analysis (Brown et al., 2006; Suzuki and Shimodaira, 2006). The classes that consisted of robustly clustered mutants were identified using the approximately unbiased (AU) P-value, which was calculated by multi-scale bootstrap resampling (Suzuki and Shimodaira, 2006). I applied this validation method to my clustering data, thereby confirming the results.

Fifth and lastly, in the past, there have been no suitable methods for the extraction of the characteristic phenotypes of individual classes. To select the characteristic parameters, I estimated the probability of the coherency of changed parameters among the mutants in the identified classes. I discovered that the distribution of the sum of the modified U statistics in each class followed the theoretical distribution of the U statistic. As a result, at $P < 0.01$, many parameters that were coherently changed by Ca^{2+} were detected in each class (Figure 7).

Morphological Changes in *cls* Mutants Caused by a High Concentration of Extracellular Ca^{2+}

A high concentration of extracellular Ca^{2+} induced various morphological changes in the wild-type yeast strain (Figure 2). In the wild-type, 13% of the parameters (65/501) were detected at $P < 0.01$

between the two conditions for ten treated samples (Table 1). This is a strikingly high number of affected parameters, since deletion mutants with the same or more levels of morphological alteration (33/254) numbered 92, which represents < 2% of the 4718 nonessential mutants (Ohya et al., 2005). In addition, the effects of a high concentration of extracellular Ca^{2+} on morphological properties were extremely variable, with changes in cell shape, position of the nucleus, location of actin patches, angle of budding, and wideness of neck.

It should be noted that the Ca^{2+} responses of the *cls* mutants varied more than those of the wild-type. The number of significantly changed parameters for all the *cls* mutants for the two conditions (Figure 3) was at least 10-fold higher than that of the wild-type, which indicates that a greater variety of morphological changes occurs in the *cls* mutants. In other words, the use of a comprehensive set of *cls* mutants enabled the discovery of a higher number of different responses to Ca^{2+} .

Some of the *cls* mutants were robustly clustered by the nature of morphological change induced by Ca^{2+} . In Class I, which included the wild-type, the nuclei of the mutants were larger (Figure 9A and 8a). The mutants of Class VII were *VMA* mutants, which are known to be functionally related. The common phenotypic change to larger cells in this class was consistent with the previously reported phenotype of *VMA* mutants (Zhang et al., 1998). In addition, in this class, decreased actin localization was observed (Figure 9C and 8f). Actin delocalization was also observed in Classes II, VI, and VII, whereas no actin parameters were detected in the wild-type for the two conditions for five treated samples ($P < 0.01$). Class VI mutants comprised Class C *VPS*

mutants, which are also known to be functionally related (Rieder and Emr, 1997). Class III mutants, which appeared as small cells when grown in a high concentration of Ca^{2+} , are iron ion transporter mutants (Kwok et al., 2006). None of the detected classes included the *cls2/csg2* mutant, which functions in releasing Ca^{2+} from the lumen of the ER (Takita et al., 1995). These results suggest that the various intensities and patterns of Ca^{2+} -induced morphological changes in *cls* mutants depend on the gene functions.

The observation of an elongated bud under high Ca^{2+} conditions in the *zds1* mutant cell (Mizunuma et al., 1998) is one of the morphological changes reportedly induced by Ca^{2+} . I confirmed that the *zds1* mutant formed elongated buds, since the parameter of C114_C (bud axis ratio of budded cell with two nuclei) was significantly increased after Ca^{2+} treatment of the five samples ($P < 0.01$). However, the bud morphology of the *cls* mutants with exception of class V *cls* mutants was coherently round rather than elongated in the presence of a high concentration of Ca^{2+} (Figure 9D, 8). It should also be noted that no *cls* mutants were robustly clustered with the *zds1* mutants. These results imply that the *CLS* genes of the seven classes are involved in pathways distinct from that of *ZDS1*.

Foresights

In the present study, I showed various effects of Ca^{2+} on yeasts using high-dimensional and quantitative phenotypic approaches. This morphological phenotyping of *cls* mutants may enable us to obtain the clues to multiple Ca^{2+} -regulatory pathways including Ca^{2+} signaling pathway,

Ca^{2+} -sensing mechanism, cytoskeleton organization, intracellular Ca^{2+} homeostasis, Ca^{2+} -mediated stress response and Ca^{2+} -dependent proteolytic system. Current method with the modified *U* statistic facilitates further phenotypic analysis of microarray data. For example, if the expression data on yeasts grown in the presence of Ca^{2+} , sodium or calcineurin inhibitor are compared with the corresponding morphological data collected under the same conditions, new insights may be obtained into the role of Ca^{2+} in yeasts (Yoshimoto et al., 2002). The expression of gene function can also be analyzed by tracing the morphological phenotypes of mutants, given that my quantitative phenotypic analysis monitors the intensities of changes caused by mutation. If the phenotypes of cells with loss of gene function are analyzed multilaterally against the proteomic information, a new phase of 'omics' research may emerge.

FIGURE LEGENDS

Figure 1. The 59 mean parameters showing differences between the effects of high and low concentrations of Ca^{2+} on wild-type yeast cells. The parameters are listed after hierarchical clustering using the Spearman rank order correlation coefficient as dissimilarity. Red and green boxes indicate the parameters that show higher and lower values under the high concentration of Ca^{2+} condition than under the low concentration of Ca^{2+} condition, respectively. Magenta and navy diamonds indicate the parameter values of ten experiments in the presence of high and low concentrations of Ca^{2+} , respectively. The minimum and maximum values of twenty experiments are also indicated. The light-green, light-red, and light-blue boxes in the ‘related morphology’ column indicate parameters that are derived from the cell wall, actin, and DNA staining, respectively. The A, A1B and C in the ‘stage’ column indicate unbudded cell, budded cell with single nucleus, and budded cell with two nuclei, respectively.

Figure 2. Illustration of morphological changes induced by extracellular Ca^{2+} in wild-type cells. The $+\text{Ca}^{2+}$ and $-\text{Ca}^{2+}$ designations indicate high and low concentrations of Ca^{2+} in the medium, respectively. The light-orange, blue, and red circles in the yeast cells indicate the cell wall, nucleus, and actin, respectively.

Figure 3. Number of significantly changed parameters in calcium-sensitive yeast strains. Samples from five independent cultures under high and low Ca^{2+} conditions were characterized by

triple-staining fluorescence microscopy and automated cell imaging (Ohya et al., 2005). For each parameter, the differences between the five values obtained for the low Ca^{2+} condition and the five values obtained for the high Ca^{2+} condition were examined using the Mann-Whitney test (Mann and Whitney, 1947). The orange line indicates the number of detected parameters in the wild-type strain.

Figure 4. Cluster analysis of the *cls* mutants based on the similarities of the morphological changes. Dissimilarity indicates a positive angle (0-180°) between the vectors of 501 dimensions (see *Materials and Methods* section). Blue values indicate AU (the P-value of the approximately unbiased test using the multi-scale bootstrap technique) in the dendrogram (Lynn and Magee, 1970; Mosch and Fink, 1997; Pruyn and Bretscher, 2000; Suzuki and Shimodaira, 2006). The orange rectangles indicate robustly clustered mutant classes at $P > 0.95$. The red and green boxes indicate modified U statistics that reflect morphological differences from untreated cells. Positive and negative values of the modified U statistic are depicted in red and green, respectively. Class indicates a mutant group that shows similar Ca^{2+} -induced morphological changes.

Figure 5. Clustering of randomized data. To demonstrate the biological origins of the patterns, data transformed into the modified U statistic were clustered before and after random permutation within rows (random 1), within columns (random 2), and both (random 3) (Eisen et al., 1998). Row, *cls* mutants; Column, morphological parameters.

Figure 6. Cluster dendrogram of the *c/s* mutants based on the similarities of the morphological changes using averaged data. The data sets for each mutant obtained from five independent cultures under both conditions are respectively averaged and then the proportions are log-transformed. The clustering method is the same as in Figure 4. Blue values indicate AU (the P-value of the approximately unbiased test using the multi-scale bootstrap technique) in the dendrogram (Suzuki and Shimodaira, 2006). The orange rectangles indicate robustly clustered mutant classes at $P > 0.95$. Dissimilarity indicates a positive angle (0-180°) between the vectors of 501 dimensions (see *Materials and Methods* section).

Figure 7. Coherently changed parameters in each class. Dissimilarity indicates a positive angle (0-180°) between the vectors of 501 dimensions (see *Materials and Methods* section). Blue values indicate AU (the P-value of the approximately unbiased test using the multi-scale bootstrap technique) in the dendrogram (Suzuki and Shimodaira, 2006). The orange rectangles indicate robustly clustered mutant classes at $P > 0.95$ in Figure 4. The red and green boxes indicate significantly increasing and decreasing parameters at significant level of 0.01, respectively.

Figure 8. Characteristic morphological changes in each class. **a-g** represent lists of parameters that show characteristic changes in class I-VII, respectively. The red and green colors in the ‘ID’ column indicate increases and decreases in parameter values following Ca^{2+} treatment at $P < 0.01$,

respectively. Dissimilarity indicates the value based on the rank-order correlation coefficient (see *Materials and Methods* section).

Figure 9. 2D plots of coherently changed parameters in each class. Color areas of yellow, pink, cyan, green, purple, orange and blue indicate distribution area of parameters in mutants of class I, II, III, IV, V, VI and VII, respectively. Gray circles and a light green diamond indicate U' values of parameters in non-classified mutants and the *zds1* mutant, respectively. U' values were calculated from two sets (high and low concentrations of Ca^{2+}) of five values for each parameter (see *Materials and Methods* section). Positive and negative values in each axis indicate increase and decrease of parameter values by Ca^{2+} treatment, respectively. Absolute value of U' equal to or higher than 12.5 and 10.5 indicates significant change in each parameter of each mutant by Ca^{2+} treatment at $P < 0.01$ and 0.05 that corresponds to P -value of U test, respectively. Cell cycle stage (A, A1B and C) is described in Figure 1 legend. A) D174_C (maximal distance between nuclear gravity center and nuclear outline in bud) and C123 (small bud ratio to budded cells). Parameter value of class I mutants (yellow diamonds) coherently increased by Ca^{2+} treatment ($P < 0.01$) (Figure 8). B) C115_A (whole cell axis ratio) and C103_A (long axis length in whole cell). Parameter value of class III mutants (cyan diamonds) coherently decreased in these parameters by Ca^{2+} treatment at significant level of 0.01. C) A112 (cells without localized actin pathes in mother) and C101_A1B (whole cell size). Parameter values of the mutants of classes II, VI and VII (pink, orange and blue squares, respectively) coherently decreased in A112 and increased in C101_A1B

by Ca^{2+} treatment at significant level of 0.01. D) Bud axis ratio in budded cells with one nucleus (C114_A1B) and that in budded cells with two nuclei (C114_C). C114_C value was significantly increased by Ca^{2+} treatment in *zds1* mutant (a light green diamond) at significant level of 0.01 with *U* test, whereas coherently decreased in Class I, II, III, IV and VII mutants (yellow, pink, cyan, green, orange and blue squares, respectively). Additionally, C114_A1B value was coherently decreased in all class except class V (purple squares) at $P < 0.01$.

Table 1. List of yeast strains used in this study.

Strain	Genotype
BY4741	<i>MATa his3Δ1 leu2Δ0 met15Δ0 ura3Δ0</i>
BYafg3Δ	BY4741 <i>afg3::KanMX</i>
BYbud25Δ	BY4741 <i>bud25::KanMX</i>
BYbud32Δ	BY4741 <i>bud32::KanMX</i>
BYcls2Δ	BY4741 <i>cls2::KanMX</i>
BYctr1Δ	BY4741 <i>ctr1::KanMX</i>
BYcwh36Δ	BY4741 <i>cwh36::KanMX</i>
BYfet3Δ	BY4741 <i>fet3::KanMX</i>
BYfir1Δ	BY4741 <i>fir1::KanMX</i>
BYgly1Δ	BY4741 <i>gly1::KanMX</i>
BYgon7Δ	BY4741 <i>gon7::KanMX</i>
BYhis3Δ	BY4741 <i>his3::KanMX</i>
BYnot5Δ	BY4741 <i>not5::KanMX</i>
BYoch1Δ	BY4741 <i>och1::KanMX</i>
BYpdr13Δ	BY4741 <i>pdr13::KanMX</i>
BYpho85Δ	BY4741 <i>pho85::KanMX</i>
BYpkr1Δ	BY4741 <i>pkr1::KanMX</i>

BY <p><i>pmc1</i>Δ</p>	BY4741 <i>pmc1::KanMX</i>
BY <p><i>pro1</i>Δ</p>	BY4741 <i>pro1::KanMX</i>
BY <p><i>psl10</i>Δ</p>	BY4741 <i>psl10::KanMX</i>
BY <p><i>rcs1</i>Δ</p>	BY4741 <i>rcs1::KanMX</i>
BY <p><i>rib4</i>Δ</p>	BY4741 <i>rib4::KanMX</i>
BY <p><i>rpl22a</i>Δ</p>	BY4741 <i>rpl22a::KanMX</i>
BY <p><i>sac1</i>Δ</p>	BY4741 <i>sac1::KanMX</i>
BY <p><i>sod1</i>Δ</p>	BY4741 <i>sod1::KanMX</i>
BY <p><i>swi3</i>Δ</p>	BY4741 <i>swi3::KanMX</i>
BY <p><i>tef4</i>Δ</p>	BY4741 <i>tef4::KanMX</i>
BY <p><i>tpd3</i>Δ</p>	BY4741 <i>tpd3::KanMX</i>
BY <p><i>trk1</i>Δ</p>	BY4741 <i>trk1::KanMX</i>
BY <p><i>ubp3</i>Δ</p>	BY4741 <i>ubp3::KanMX</i>
BY <p><i>vma1</i>Δ</p>	BY4741 <i>vma1::KanMX</i>
BY <p><i>vma2</i>Δ</p>	BY4741 <i>vma2::KanMX</i>
BY <p><i>vma3</i>Δ</p>	BY4741 <i>vma3::KanMX</i>
BY <p><i>vma4</i>Δ</p>	BY4741 <i>vma4::KanMX</i>
BY <p><i>vma5</i>Δ</p>	BY4741 <i>vma5::KanMX</i>
BY <p><i>vma6</i>Δ</p>	BY4741 <i>vma6::KanMX</i>

BYvma7Δ	BY4741 vma7::KanMX
BYvma8Δ	BY4741 vma8::KanMX
BYvma10Δ	BY4741 vma10::KanMX
BYvma11Δ	BY4741 vma11::KanMX
BYvma12Δ	BY4741 vma12::KanMX
BYvma13Δ	BY4741 vma13::KanMX
BYvma16Δ	BY4741 vma16::KanMX
BYvma21Δ	BY4741 vma21::KanMX
BYvma22Δ	BY4741 vma22::KanMX
BYvps11Δ	BY4741 vps11::KanMX
BYvps15Δ	BY4741 vps15::KanMX
BYvps16Δ	BY4741 vps16::KanMX
BYvps18Δ	BY4741 vps18::KanMX
BYvps33Δ	BY4741 vps33::KanMX
BYvps34Δ	BY4741 vps34::KanMX
BYvps36Δ	BY4741 vps36::KanMX
BYvps45Δ	BY4741 vps45::KanMX
BYwhi3Δ	BY4741 whi3::KanMX
BYyel045cΔ	BY4741 yel045c::KanMX

BY <i>ykl118w</i> Δ	BY4741 <i>ykl118w::KanMX</i>
BY <i>yor331c</i> Δ	BY4741 <i>yor331c::KanMX</i>
BY <i>ypr099c</i> Δ	BY4741 <i>ypr099c::KanMX</i>
BY <i>zap1</i> Δ	BY4741 <i>zap1::KanMX</i>
BY <i>zds1</i> Δ	BY4741 <i>zds1::KanMX</i>
BY <i>zuol</i> Δ	BY4741 <i>zuol::KanMX</i>

All of mutants were purchased from EUROSCARF. The mutants excluding *his3* and *zds1* were isolated as *cls* mutant by Kanai.

Table2. The significantly changed parameters of wild-type under containing high-concentration of Ca^{2+} .

ID	Description	P-value
1. Parameters where values significantly increased		
C115_A	Whole cell axis ratio	1.083E-05
CCV103_C	Coefficient of variation of C103_C	1.083E-05
CCV115_A	Coefficient of variation of C115_A	1.083E-05
CCV12-1_C	Coefficient of variation of C12-1_C	1.083E-05
D107_A1B	Ratio of D104 to C103	1.083E-05
CCV103_A1B	Coefficient of variation of C103_A1B	2.165E-05
D148_A1B	Relative distance of nuclear brightest point to mother center	2.165E-05
D154_A	Angle between C1D1-1 and C1C1-2	2.165E-05
C115_A1B	Mother axis ratio	4.330E-05
C115_C	Mother axis ratio	4.330E-05
D147_A1B	Relative distance of nuclear gravity center to mother center	4.330E-05
C13_A	Whole cell fitness for ellipse	7.578E-05
CCV102_C	Coefficient of variation of C102_C	7.578E-05
D104_A1B	Distance between nuclear gravity center and mother tip	7.578E-05
D110_A1B	Distance between nuclear gravity center and middle point of neck	7.578E-05

D114_A1B	Ratio of D110 to C128	7.578E-05
DCV154_A	Coefficient of variation of D154_A	7.578E-05
C114_C	Bud axis ratio	1.299E-04
CCV110_A1B	Coefficient of variation of C110_A1B	1.299E-04
D105_A	Ratio of D102 to C103	1.299E-04
D118_A1B	Distance between nuclear gravity center and mother center	1.299E-04
D129_A1B	Distance between nuclear brightest point and mother tip	1.299E-04
D152_A1B	Mobility of nucleus in mother	1.299E-04
D169_A1B	Angle between C4-1D1-1 and C4-1C1	1.299E-04
DCV147_A1B	Coefficient of variation of D147_A1B	1.299E-04
CCV106_A1B	Coefficient of variation of C106_A1B	2.057E-04
CCV112_C	Coefficient of variation of C112_C	2.057E-04
CCV114_C	Coefficient of variation of C114_C	2.057E-04
D170_A1B	Angle between C4-1D2-1 and C4-1C1	2.057E-04
DCV148_A1B	Coefficient of variation of D148_A1B	2.057E-04
D132_A1B	Distance between nuclear brightest point and middle point of neck	3.248E-04
CCV116_C	Coefficient of variation of C116_C	4.871E-04
D142_A1B	Distance between nuclear brightest point and mother hip	4.871E-04
D155_A	Angle between C1D2-1 and C1C1-2	4.871E-04

CCV11-1_C	Coefficient of variation of C11-1_C	7.253E-04
CCV12-1_A1B	Coefficient of variation of C12-1_A1B	7.253E-04
D126_A1B	Distance between nuclear gravity center and mother hip	7.253E-04
D169_C	Angle between C4-1D1-1 and C4-1C1	7.253E-04
C106_A1B	Bud direction	1.050E-03
D163_C	Angle between D2-1D2-2 and C1C4-1	1.050E-03
D170_C	Angle between C4-1D2-1 and C4-1C1	1.050E-03
DCV155_A	Coefficient of variation of D155_A	1.050E-03
D136_A1B	Distance between nuclear brightest point and mother center	1.505E-03
C13_A1B	Mother cell fitness for ellipse	2.089E-03
CCV101_A1B	Coefficient of variation of C101_A1B	2.089E-03
D162_C	Angle between D1-1D1-2 and C1C4-1	2.089E-03
DCV114_A1B	Coefficient of variation of D114_A1B	2.089E-03
CCV102_A1B	Coefficient of variation of C102_A1B	2.879E-03
CCV128_C	Coefficient of variation of C128_C	2.879E-03
DCV105_A	Coefficient of variation of D105_A	2.879E-03
ACV101_A1B	Coefficient of variation of A101_A1B	3.886E-03
C110_A1B	Distance between bud tip and mother long axis extension	3.886E-03
CCV101_C	Coefficient of variation of C101_C	3.886E-03

D145_A1B	Distance between nuclear outline point D7 and mother hip	3.886E-03
D145_C	Distance between nuclear outline point D7 in mother and mother hip	3.886E-03
C13_C	Mother cell fitness for ellipse	5.196E-03
CCV11-1_A1B	Coefficient of variation of C11-1_A1B	5.196E-03
D143_A1B	Distance between nuclear outline point D6-1 and middle point of neck	5.196E-03
D148_A	Relative distance of nuclear brightest point to cell center	5.196E-03
D172_A1B	Angle between C4-1D4 and C4-1C1	5.196E-03
DCV118_A1B	Coefficient of variation of D118_A1B	5.196E-03
C114_A1B	Bud axis ratio	6.841E-03
CCV115_A1B	Coefficient of variation of C115_A1B	6.841E-03
DCV112_C	Coefficient of variation of D112_C	6.841E-03
D155_A1B	Angle between C1D2-1 and C1C1-2	8.931E-03

2. Parameter where values significantly decreased

CCV128_A1B	Coefficient of variation of C128_A1B	1.150E-02
D135_A	Distance between nuclear brightest point and cell center	1.150E-02
A7-1_C	Size of actin region in mother	1.469E-02
D127_A	Distance between nuclear brightest point and cell tip	1.469E-02
DCV119_C	Coefficient of variation of D119_C	1.469E-02
A104_C	Relative distance of actin patch center from neck in bud	1.854E-02

CCV103_A	Coefficient of variation of C103_A	1.854E-02
D141_C	Distance between nuclear brightest point in mother and mother hip	1.854E-02
D147_A	Relative distance of nuclear gravity center to cell center	1.854E-02
ACV101_A	Coefficient of variation of A101_A	2.323E-02
C109_C	Neck width	2.323E-02
D103_C	Distance between nuclear gravity center in mother and mother tip	2.323E-02
DCV113_C	Coefficient of variation of D113_C	2.323E-02
DCV149_C	Coefficient of variation of D149_C	2.323E-02
A101_A1B	Actin region ratio in whole cell	2.881E-02
A107_C	Actin c ratio	2.881E-02
CCV118_C	Coefficient of variation of C118_C	2.881E-02
D125_C	Distance between nuclear gravity center in mother and mother hip	2.881E-02
D128_C	Distance between nuclear brightest point in mother and mother tip	2.881E-02
D146_C	Distance between nuclear outline point D8 in bud and bud tip	2.881E-02
DCV143_A1B	Coefficient of variation of D143_A1B	2.881E-02
C105_A1B	Neck position	3.546E-02
C127_A1B	Thickness difference of cell wall	3.546E-02
D121_C	Distance between nuclear gravity center in bud and bud tip	3.546E-02
DCV137_C	Coefficient of variation of D137_C	3.546E-02

ACV7-1_A	Coefficient of variation of A7-1_A	4.326E-02
ACV7-1_A1B	Coefficient of variation of A7-1_A1B	4.326E-02
C107_C	Long axis length in bud	4.326E-02
C109_A1B	Neck width	4.326E-02
CCV105_A1B	Coefficient of variation of C105_A1B	4.326E-02
CCV109_C	Coefficient of variation of C109_C	4.326E-02
D102_A	Distance between nuclear gravity center and mother tip	4.326E-02
D154_C	Angle between C1D1-1 and C1C1-2	4.326E-02
D182_A	Nuclear axis ratio	4.326E-02
DCV150_C	Coefficient of variation of D150_C	4.326E-02

P-values were estimated by applying the *U*-test to the samples of 10 vs 10 obtained from independent cultures under conditions of low- and high-concentration of Ca^{2+} , respectively.

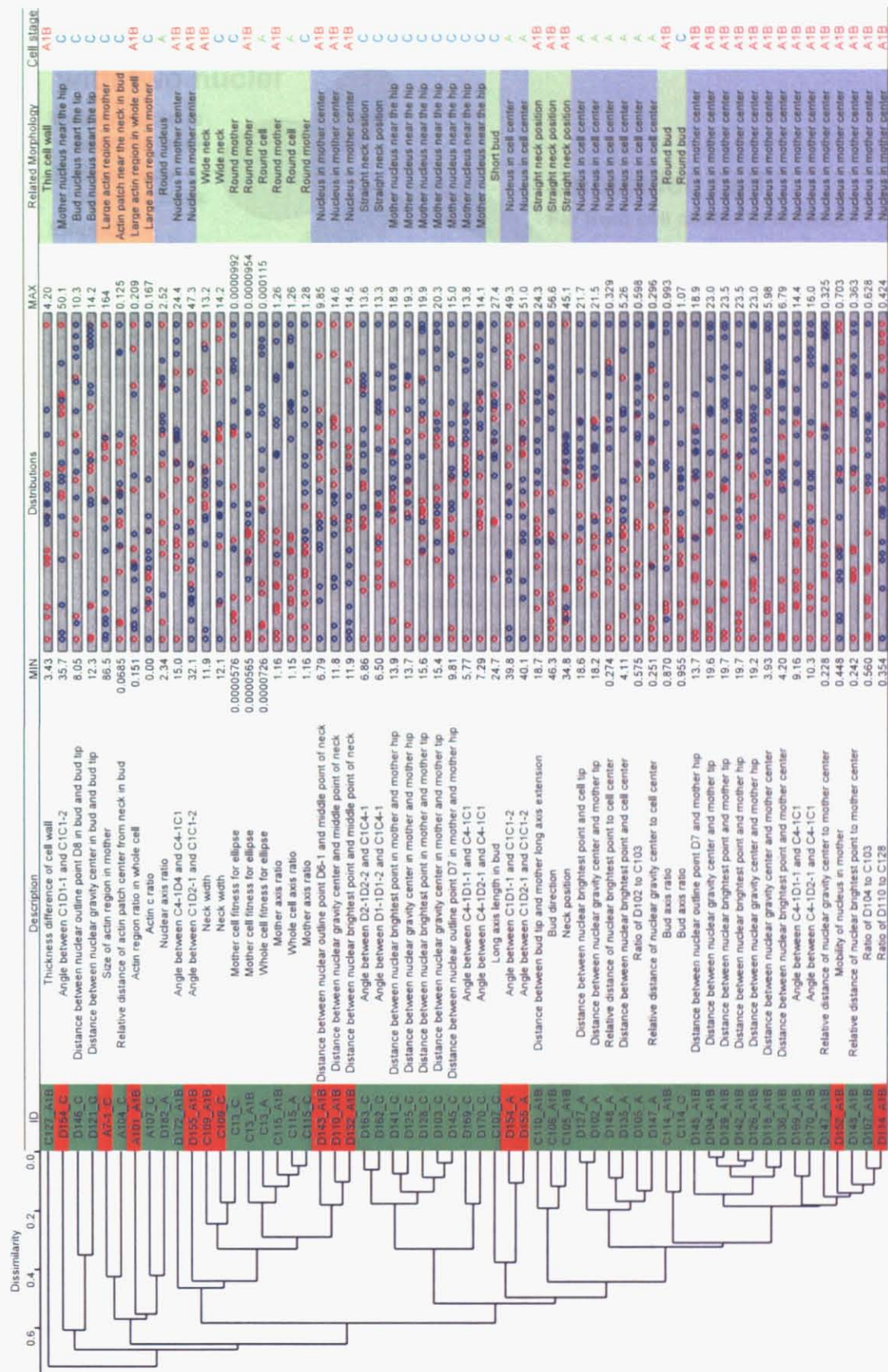


Figure 1.

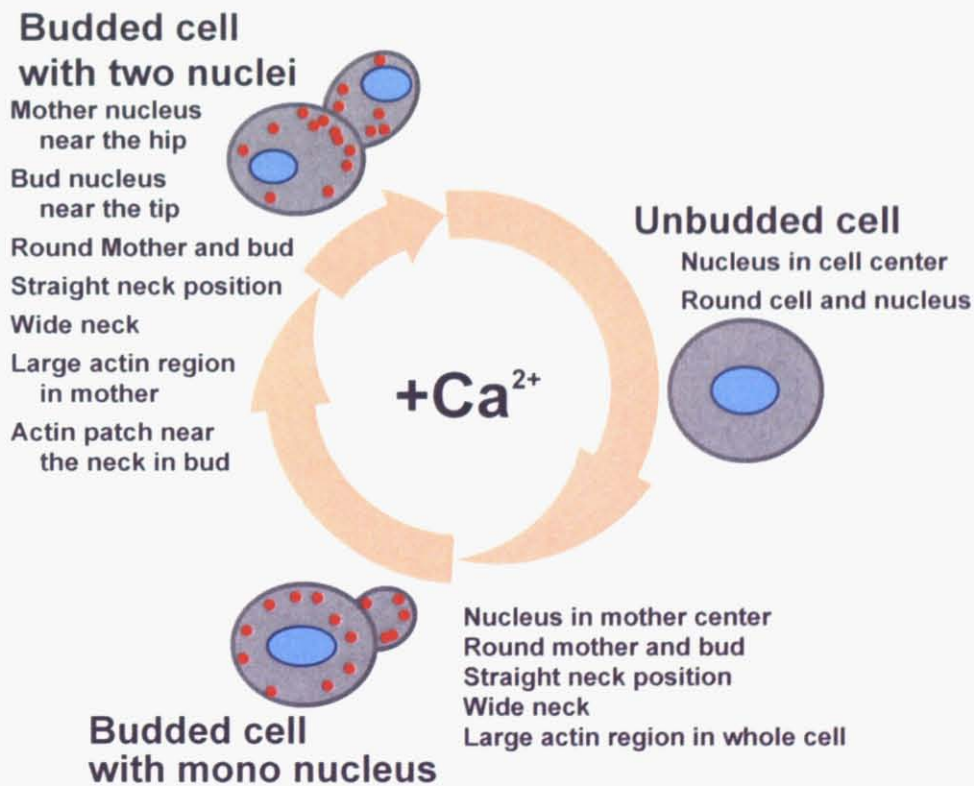
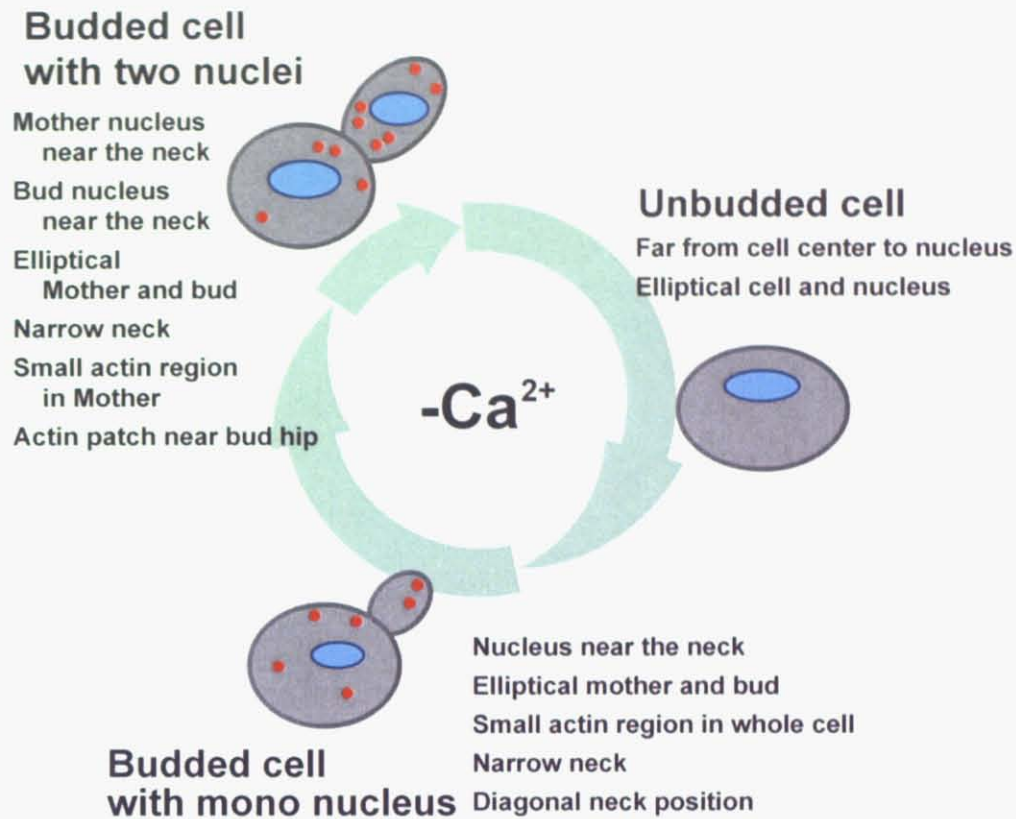


Figure 2.

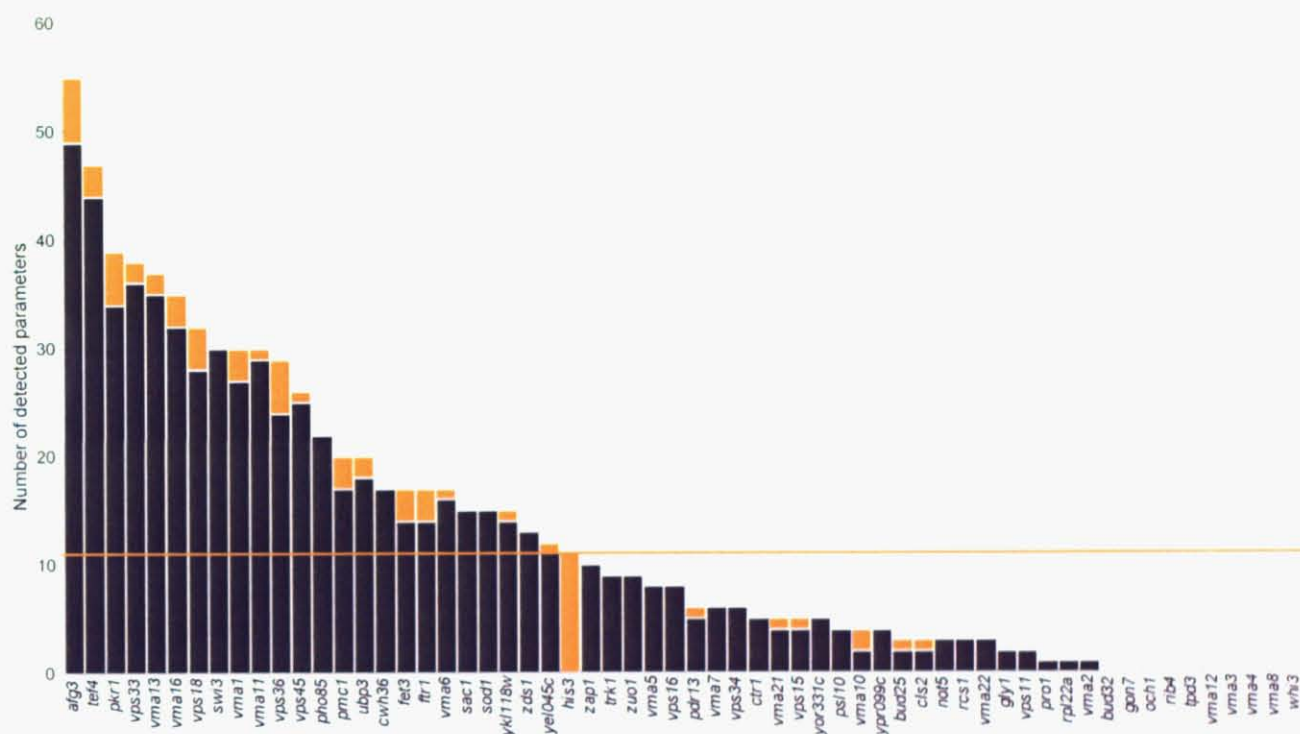


Figure 3.

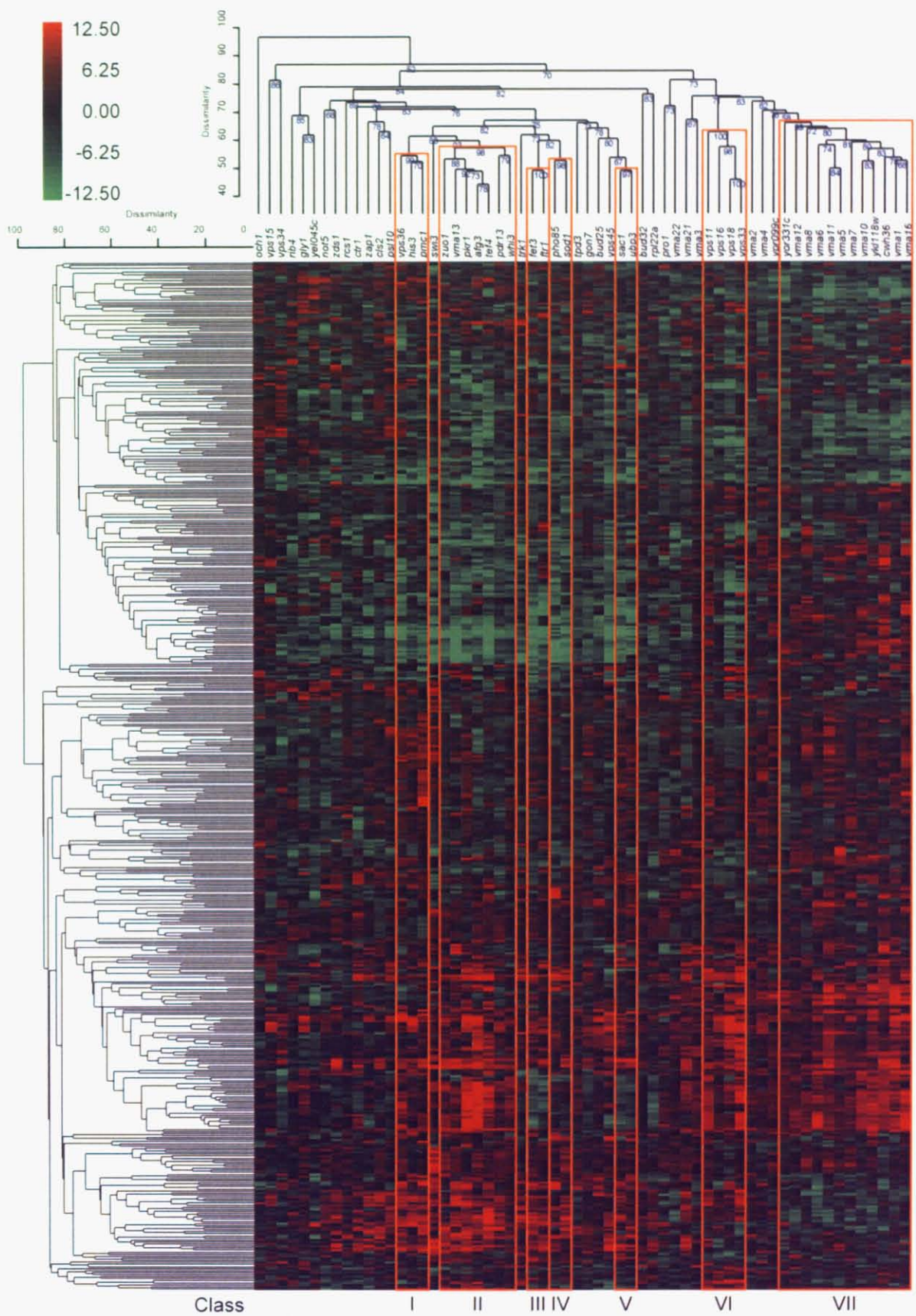


Figure 4.

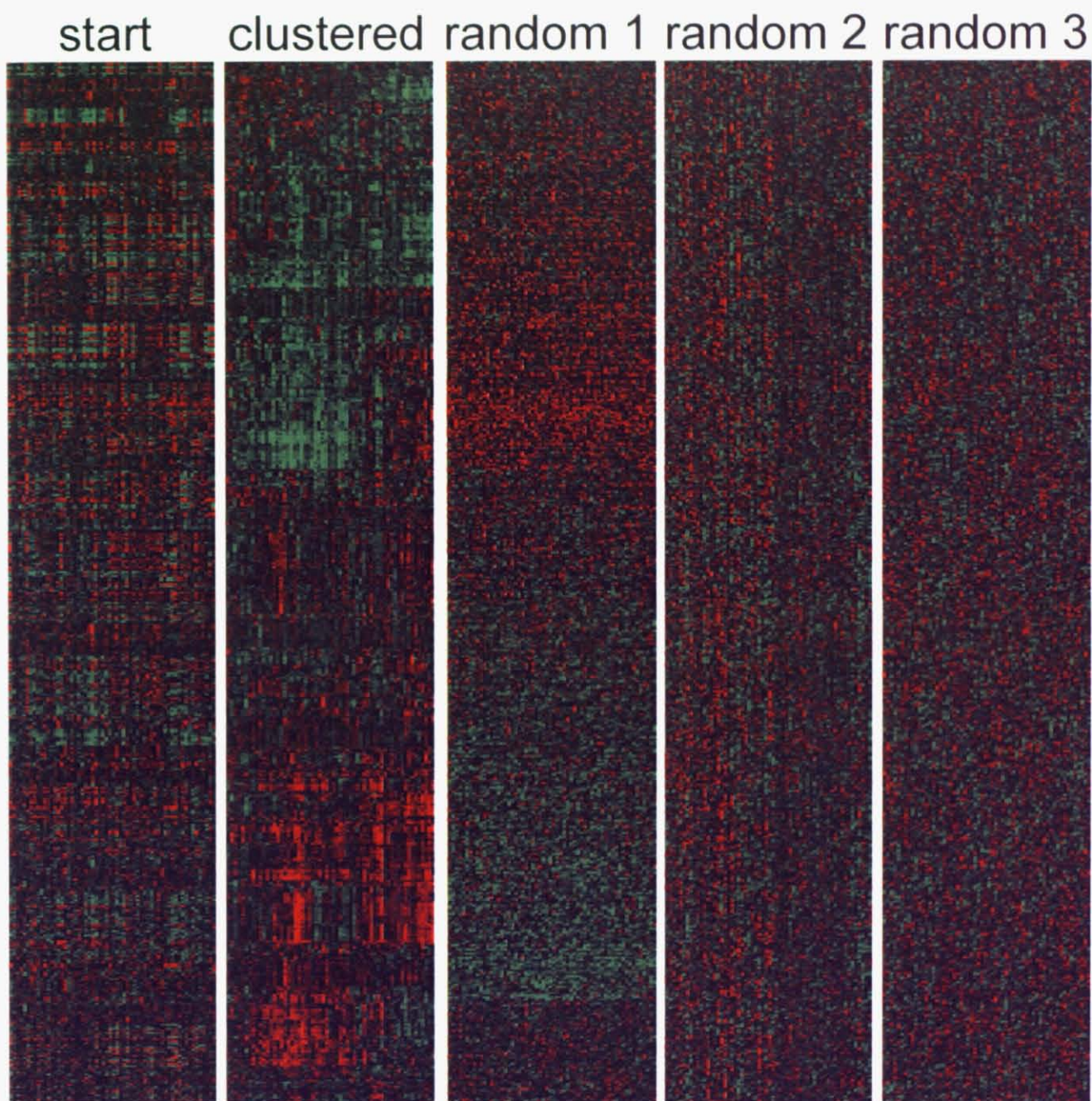


Figure 5.

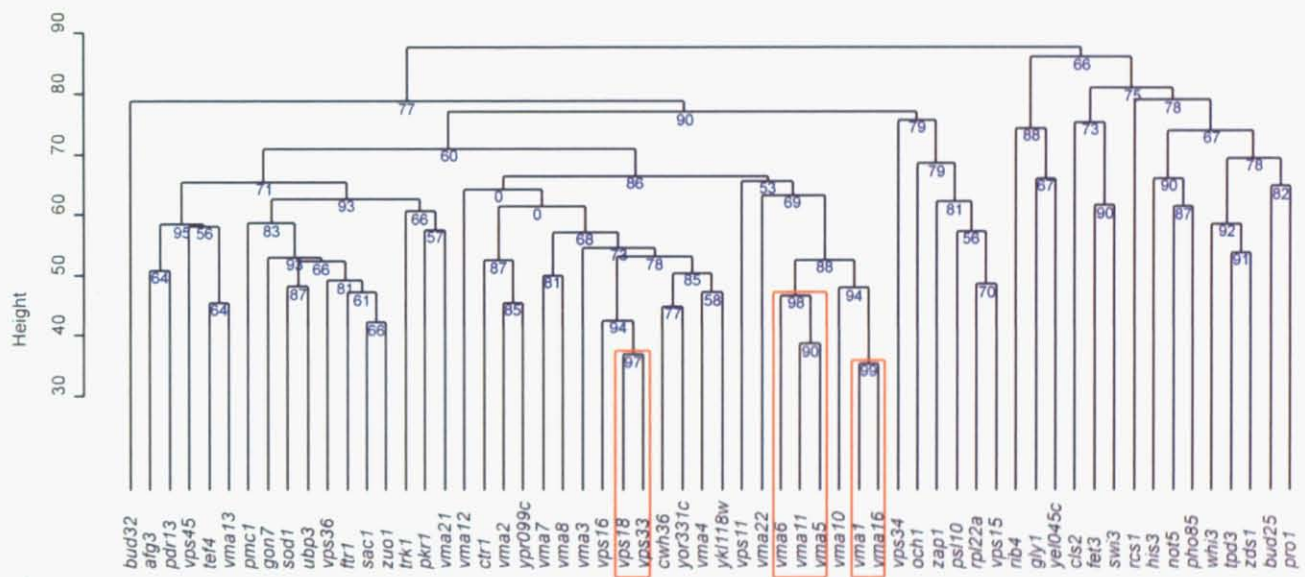


Figure 6.

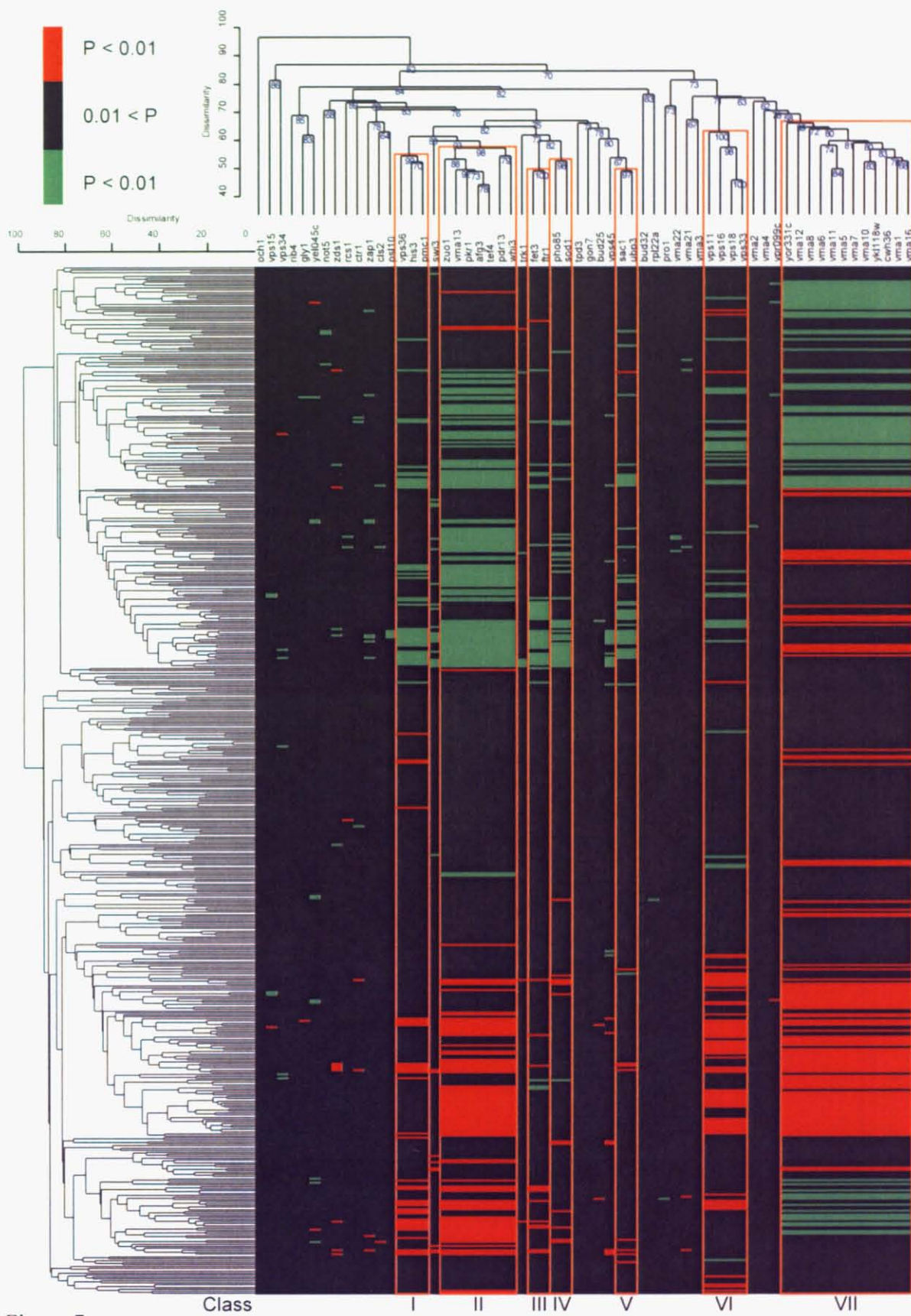


Figure 7.

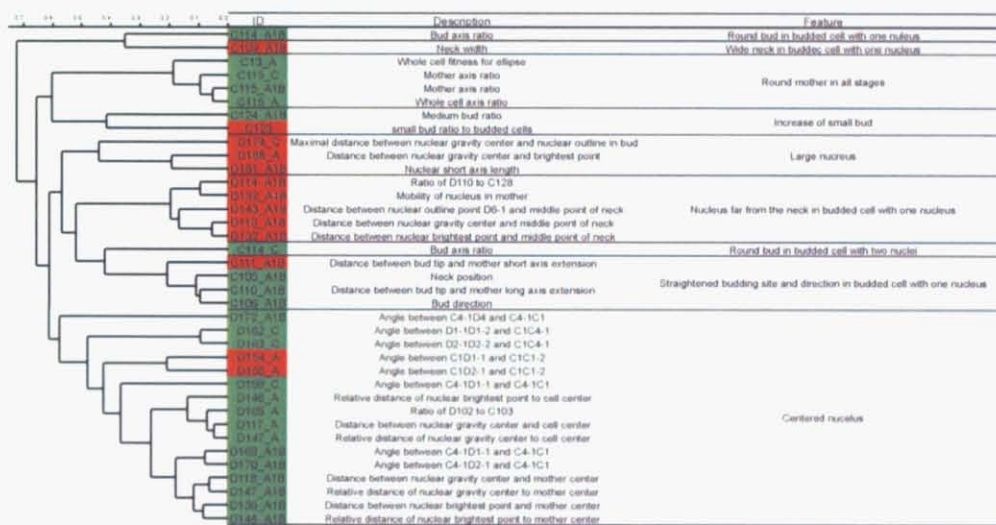


Figure 8a. Class I

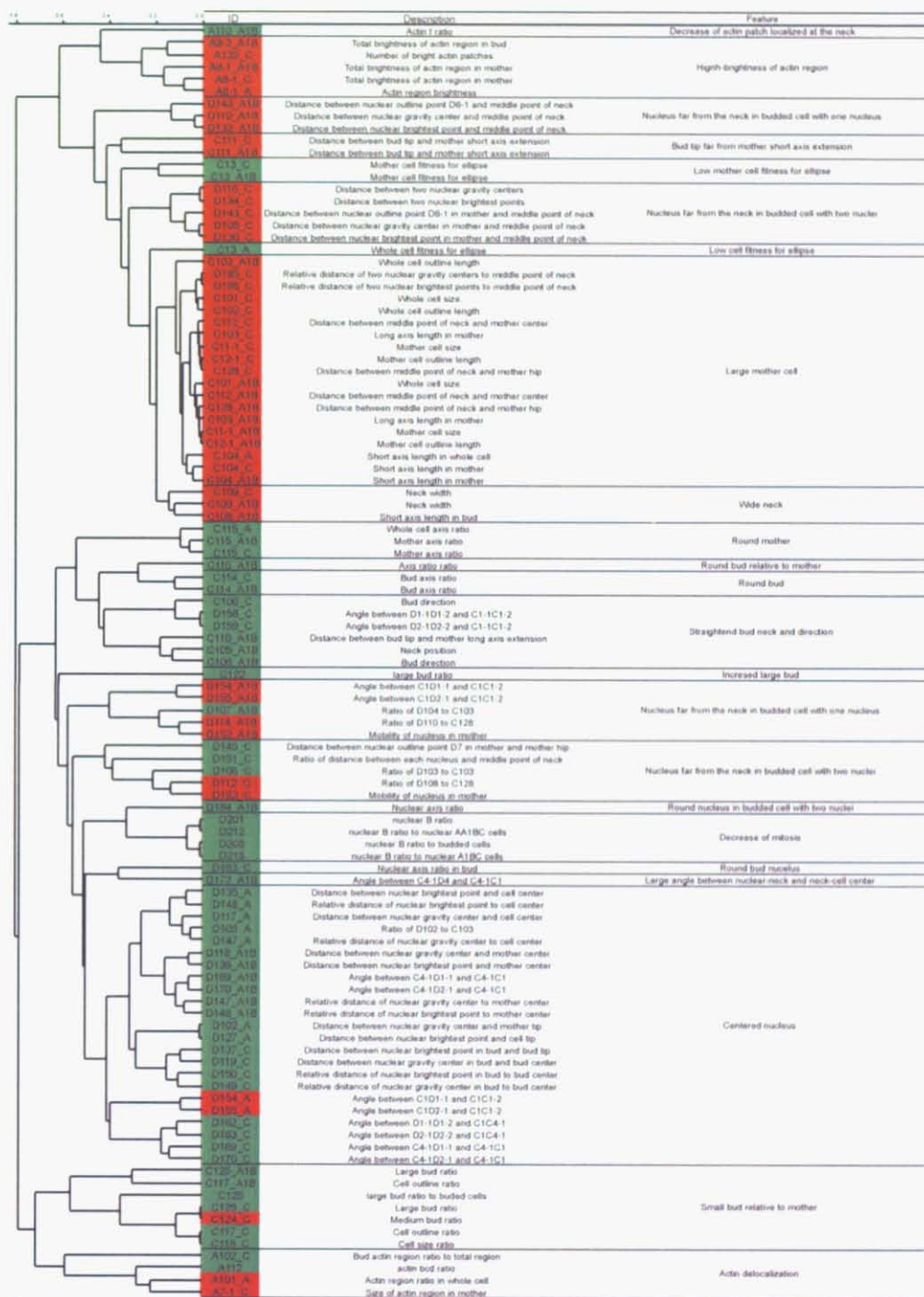


Figure 8b. Class II

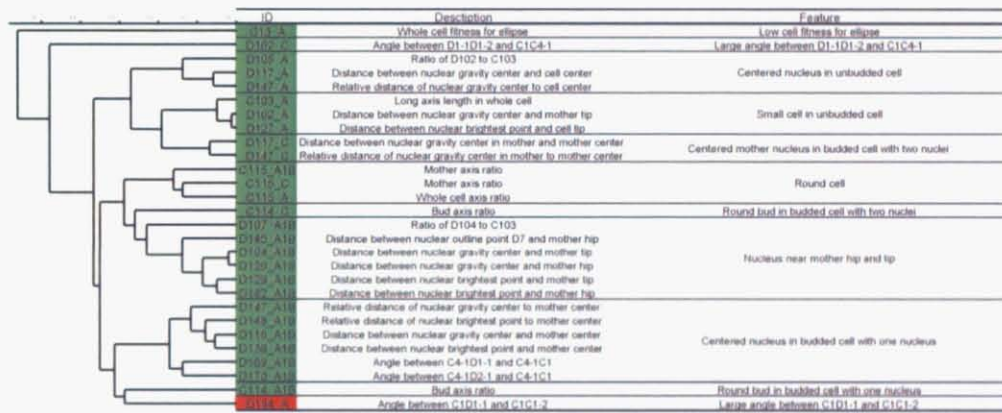


Figure 8c. Class III

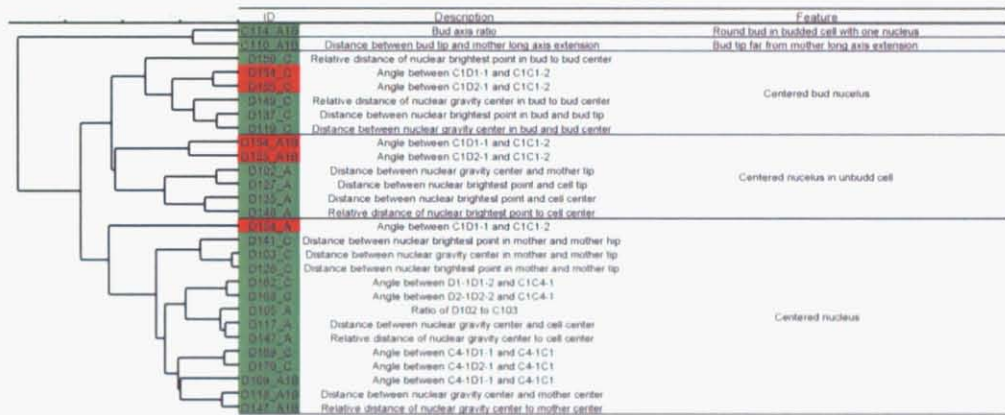


Figure 8d. Class IV

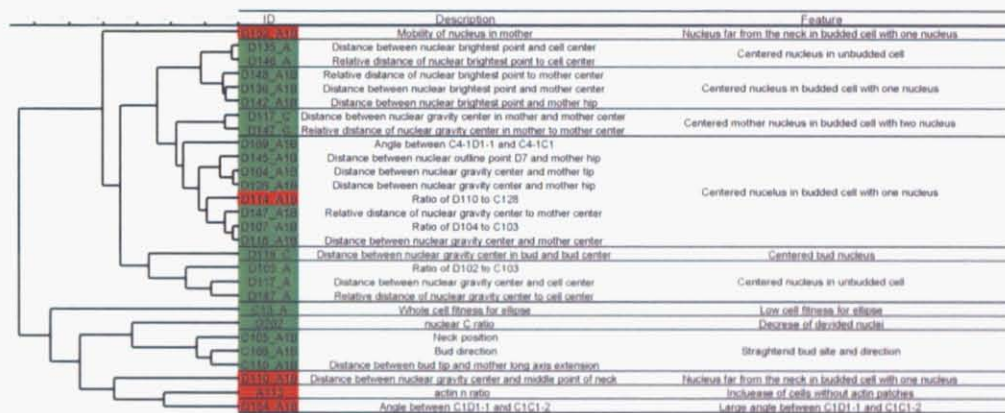


Figure 8e. Class V

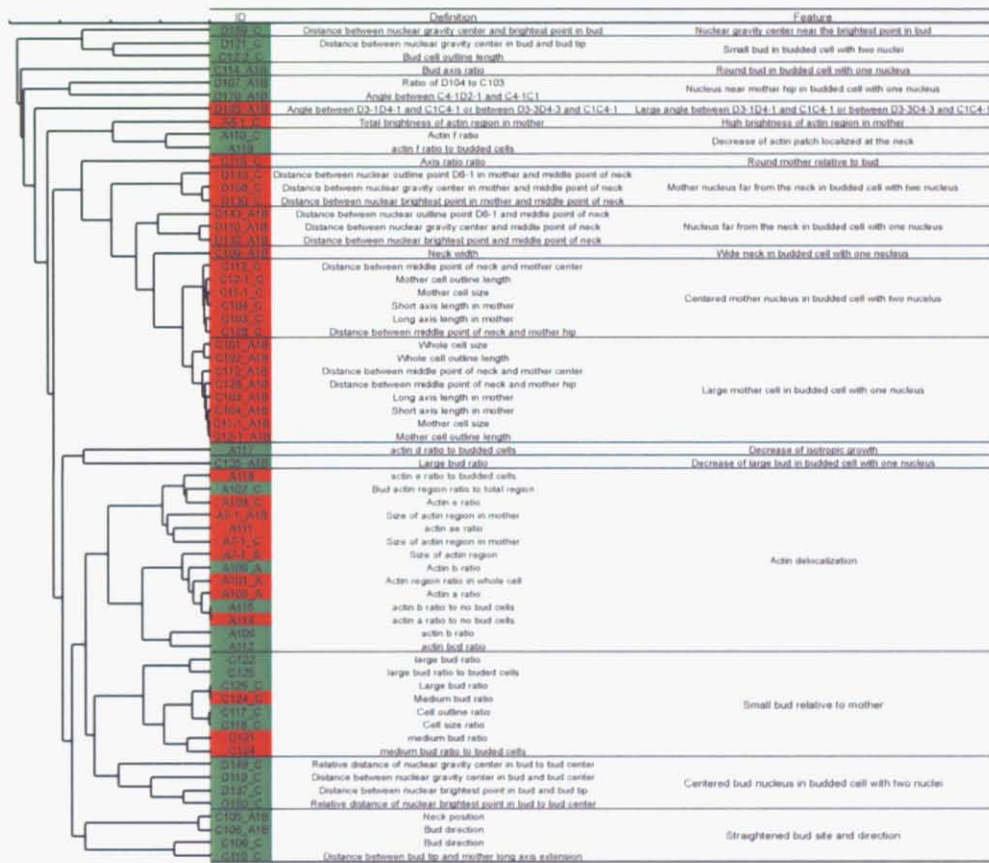
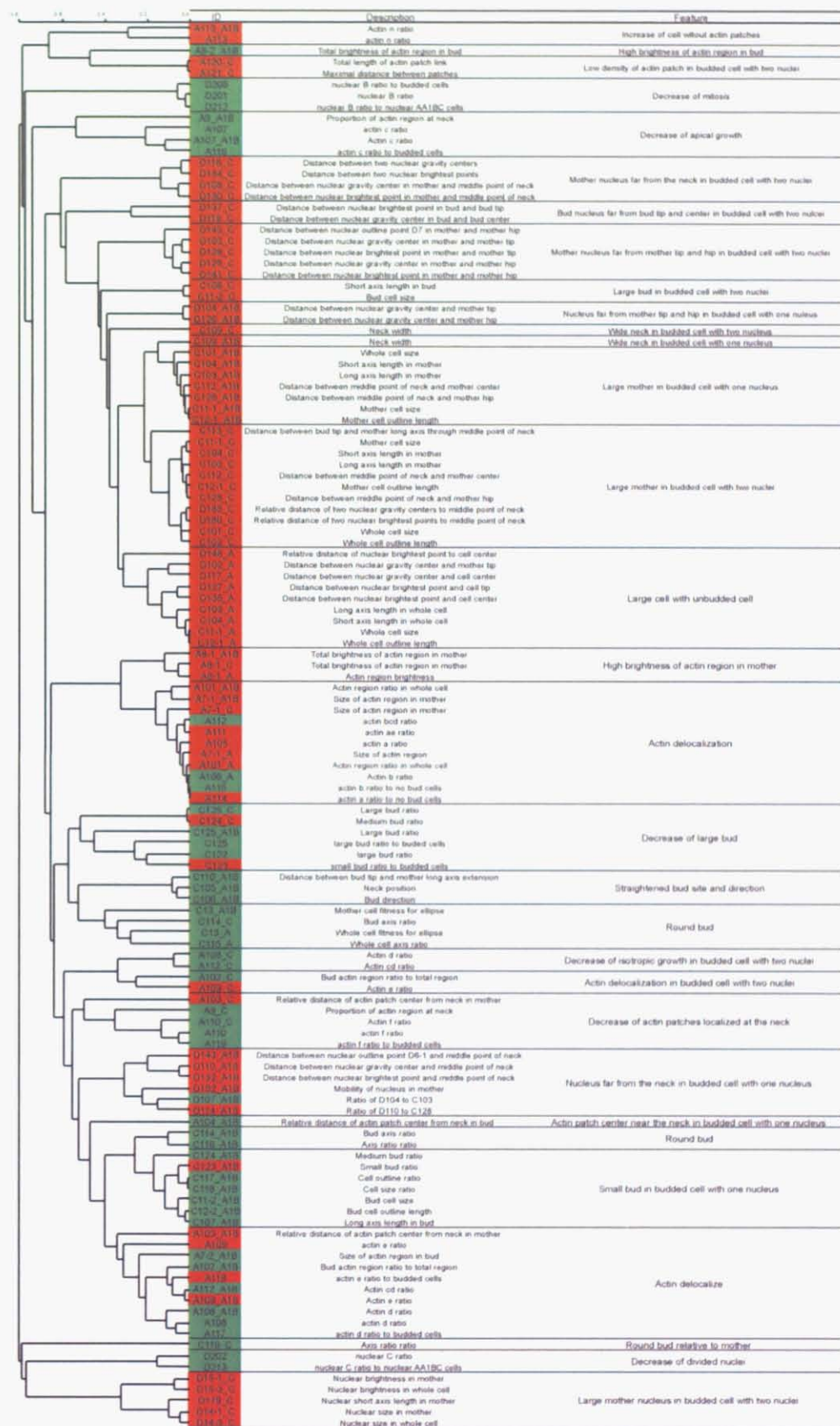


Figure 8f. Class VI



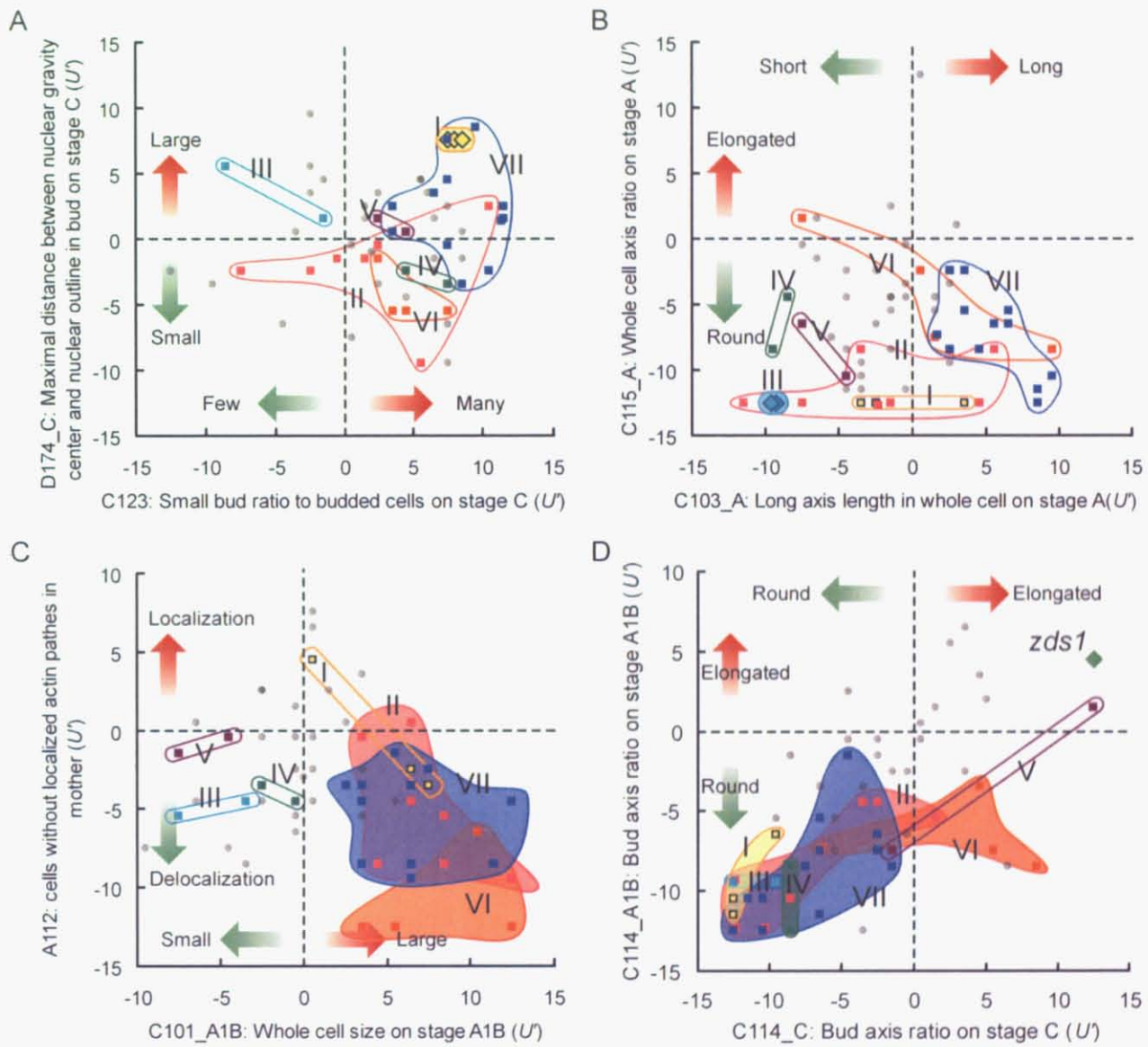


Figure 9.

CHAPTER 2.

Feasibility study of high-throughput microphotography system using microfluidics

INTRODUCTION

As shown in the previous chapter, replicated experiments enable us to cluster mutants by morphological similarity (Figure 4) and to identify morphological feature of mutants which are in the same class (Figure 7). However, the replicated experiments require much time and many costs, especially in the process from cell culture to obtaining microphotograph that follows conventional and time-consuming methods although CalMorph achieved high-throughput analysis (Ohya et al., 2005). Three steps should be improved to break through the limitation of time and cost; cell culture, cell staining, and microscopic observation. Among them, I focus on development of high-throughput microphotography system, because the process of microscopic observation is rate-limiting step; maximum number of samples that can be photographed is 30 per expert per week, whereas more samples of cell culture and cell staining can be processed.

To develop the high-throughput microphotography system, I employed on microfluidics based on PDMS (polydimethylsiloxane). The microfluidics is the science and technology of systems that process or manipulate small (10^{-9} to 10^{-18} litres) amounts of fluids, using channels with dimensions of tens to hundreds of micrometers, which dimensions are well suited for treating eukaryotic cells including yeast cells (Whitesides, 2006).

The microfluidics offer a number of useful capabilities: the ability to use very small quantities of samples and reagents, and to carry out separations and detections with high resolution

and sensitivity; low cost; and short times for analysis (Manz et al., 1992). The microfluidics exploits both its most obvious characteristic small sized and less obvious characteristics of fluids in microchannels, such as laminar flow (Fujii et al., 2003). It offers fundamentally new capabilities in the control of concentrations of molecules in space and time (Whitesides, 2006). These features of microfluidics may enable to scale-down the CalMorph image processing system and speed-up the microphotograph acquisition.

PDMS is one of the most frequently used elastometric materials in fabricating the microfluidic devices. The devices are relatively easy to fabricate by soft lithography rather than rigid materials (conventional silicon or glass) and are compatible with most biological assays (El-Ali et al., 2006). The easy fabrication by elastomers enable to fabricate the components required for microanalytical systems, especially pumps and valves (Ng et al., 2002). PDMS - with its excellent optical transparency, low toxicity and high permeability to dioxygen and carbon dioxide - is a material that is probably uniquely suitable as a medium for the fabrication of microchambers (Balagadde et al., 2005). These features of microfluidics may enable to do experiment under versatile conditions and obtain fluorescence and bright-field microphotograph at high-magnification.

In this chapter, I designed a microfluidic chip to test for suitability of microfluidics for our CalMorph image processing system. High-magnification photograph of yeast cells on microfluidic chip could be obtained and outline of yeast cell wall were recognized by CalMorph designed for phase-contrast images. Cell morphology obtained from images on microfluidic chip are similar to

that on conventional slide glass, therefore the feasibility for development of high-throughput microphotography system was confirmed.

MATERIALS AND METHODS

Chip Fabrication and Handling

Based on my fabrication drawing, microfluidic chip was fabricated by Fluidware technologies Inc. Microchannels were cleaned with cell lysis solution (0.2 mg/ml Zymolyase, SEIKAGAKU CORPORATION), 1% (w/v) NP40 detergent and purified water. The solutions injected by syringes into the microchannels were filtrated with syringe filter of pore size 0.45 μm (CORNING). The chip was cleaned with bath-type sonicator (BRANSON).

Media and Strains

Strain used was BY $his3\Delta$ (Table 1). The media, culture condtion, and cell fixation are described in Materials and Methods of CHAPTER I.

Quantitative phenotypic analysis

Phase-contrast images of simply fixed yeast cells on the slide-glass and on the chip were acquired with a Zeiss Axiophot2 imaging microscope ($\times 100$ objective). Then image-processing program (Ohtani et al., 2004) designed for phase-contrast image was applied to the images to obtain quantitative morphological data. Brightness difference between cells and background of the images from the microfluidic chip was fitted to more than 60 by using Photoshop CS2 (Adobe). 19 of morphological parameters (Table 4) are available when only phase-contrast images are analyzed. The differences between the two conditions of these parameter values of each cell were assessed by

Mann-Whitney's U-test at significant level of 0.05 (Mann and Whitney, 1947).

RESULTS

Chip design

To examine whether yeast cells placed in the microfluidic chip can be observed on the microscopy, I designed simply straight microchannels. Several microchannels different in width were designed for examining the suitability for manipulating and observing yeast cells; visual field height of microphotograph is about 67 μm therefore the five microchannel widths were designed to from 40 to 80 μm (Figure 10A). Silicon tubes out from inlets and outlets of microchannels were designed for continuously injecting and manipulating of microfluid with syringes. The microfluidic chip made of PDMS was sandwiched between non-fluorescence glasses to be ready to use on the stage of the microscopy. The microfluidic chip (Figure 10B) fabricated by Fluidware Technologies Inc. had highly precise microchannels (Table 3).

Observation of yeast cells on the chip

Yeast cells in the microchannels were easily observed in high-magnification microscopy (Figure 11A). There were no apparent differences in cell morphology among the widths of microchannel (Figure 11A), but the narrower microchannels were, the more frequently be narrowed or blocked by aggregated cells or debris (Figure 11B). Moreover, the wider microchannels were, the more cells could be observed in a visual field of microphotograph (Figure 11A), therefore the wider microchannels were preferable for cell suspension manipulation and high-throughput microphotography.

Recognition of yeast cell outline by CalMorph

To examine whether yeast cells placed in microchannel can be used for CalMorph analysis, I tested several microfluid conditions. When the yeast cells in the microchannel were observed under the microscopy after suspended with PBS, CalMorph did not recognize their phase-contrast images (Figure 12Aa). The recognition was also failed when PBS-suspended cells were observed after placed on conventional slide glass (Figure 12Ba), suggesting that the failure is irrespective of the microchannel. On the contrary, when yeast cells were suspended with glycerol (a frequently used solvent for observation on slide-glass) and observed on the slide glass, the cell images were recognized by CalMorph (Figure 12Bb-c) (Fukuoka, 2004). I noticed that the background of cell images suspended in PBS was darker than that in glycerol. The phase-contrast microscopy forms the image by converting phase-difference to brightness, and the phase-difference depends on the refractive index (Schmitt and Kumar, 1996). Therefore, the brightness difference between cells and background is dependent on different refractive index of the solutions such as glycerol and PBS. I measured difference of mode of brightness level between cells and background in images taken under several conditions. The brightness difference in the unrecognized images (25.8 ± 10.2 , $n = 4$) was smaller than that in the recognized images (42.0 ± 13.6 , $n = 4$). It was revealed that the cell images (more than 90%) are exclusively recognized by CalMorph when the brightness difference is more than 60. Since glycerol can not be used as an injecting solvent because of its viscosity, the brightness difference of the images from the microfluidic chip was artificially fitted to more than 60 (Materials and Methods). After this data processing, cell images taken in microchannel are

successfully recognized by CalMorph (Figure 12Bc).

Compatibility of quantitative morphological data between yeast cells on the microfluidic chip and on the conventional slide glass

To examine whether quantitative morphological data taken in microchannel is reliable, I compare the morphological data between the two type of cells, PBS-suspended cells on the microfluidic chip and glycerol-suspended cells on the conventional slide-glass. Based on the cell outline images, 19 morphological parameters are computed by this version of CalMorph. The mean values of these parameters in each condition were shown in Table 4. There were no significant differences detected by *U*-test at the significant level of 0.05 between two conditions, suggesting that the quantitative morphological trait obtained by CalMorph was compatible between two conditions.

DISCUSSION

I succeeded in microscopic observation of yeast cells using microfluidic chip. I set up chip design and experimental protocol suitable for CalMorph analysis and found that morphological data between yeast cells on the chip and on the slide glass are compatible. Although my current study suggests that the microfluidic chip can be substituted for the slide glass, to establish the high-throughput microphotography system, three major problems are still remained: acquisition of fluorescence images; control of cell movement; and aggregation of cells and debris in the microchannels. These problems are further described and discussed below.

The fluorescence images of yeast cells on the chip could not be acquired because of fast fading. Conventional anti-fade reagent could not use because of viscosity. This problem may be soluble by using low-viscosity anti-fade reagents which are suitable for microchannel. Because fast fading also results in long exposure time, the cells need to be kept settled during exposure.

Movement of cells in the microchannels is problematic: images will be blurred or out of focus. I found that flowing cells were rolling when cells were in fast flow through microchannels, and each bud and cell faced various directions in various depths after the flow was slowed down, followed by sinking to the bottom and laying down in about 30 sec. Increasing the volume of microchannels, using a micropump, or using a low-melting-point agarose will be effective to control flow. Reducing the depth of microchannels is an alternative way to quickly settle cells. A technique which alter the depth of microchannel by air pressure (Unger et al., 2000) will be useful.

For high-throughput microphotography system, it is necessary to sequentially treat

different samples with the same chip. The aggregated cells and the debris seriously disturbed the observation of the cells on the chip by blocking or narrowing the microchannels. I found the cell aggregation was occurred when the flow was reversed or when the cells were accumulated at adhered cells or debris on the wall. The aggregated cells and the debris were reduced by the presonication of the cell suspension and the prefiltration of the buffers, and by using wider microchannels. Moreover, the aggregated cells could be removed by using the enzymatic cell lysis solution and/or the detergent while the microchannels were not completely blocked. Therefore, , the careful pretreatment and cleaning of the chip will be enable us to sequentially treat different samples with same chip.

I will improve this high-throughput microphotograpy system by overcoming these problems. Once the system is established, the genome-wide, statistical, high-dimensional and quantitative phenotypic analysis under highly various conditions will be possible with low cost and short time.

FIGURE LEGENDS

Figure 10. The microfluidic chip used in this study. **a)** The fabrication drawing for microfluidic chip.

b) The photogram of fabricated microfluidic chip. The microfluidic chip was fabricated by Fluidware Technologies Inc.

Figure 11. Phase-contrast images of microchannels. **A)** The yeast cells in the microchannels of 40 μm (**a**) and 80 μm (**b**) width. **B)** The aggregated cells and debris in the microchannels of 40 μm width. All images were obtained using high-magnification microscope with $\times 100$ objective lens and samples were suspended with PBS. Yeast cells were fixed at log-phase.

Figure 12. Microphotographs of yeast cells for image analysis using CalMorph. **A)** A microphotograph of PBS-suspended yeast cells in a microchannel of 40 μm width (**a**). A processed image to fit the estimated threshold (see text) successfully analyzed by CalMorph (**b**). **B)** Microphotographs of yeast cells suspended in PBS(**a**) and in glycerol(**b**) and (**c**)) on slide-glass. (**c**) is an analyzed image of the yeast cell outline of (**b**). All images were obtained by phase-contrast microscopy with $\times 100$ objective lens. Yeast cells were fixed at log-phase.

Table 3. Measurements of fabricated microchannels.

		width (μm)				depth (μm)	
Designed value		40	50	60	70	80	10
Actual measurement value							
Maximum		42	50	63	72	81	10
Minimum		39	49	62	71	81	9

Table 4. Morphological parameter values of yeast cells under each condition.

ID	Description	Slide glass	Microfluidic	unit
		(n = 11 cells)	chip (n = 21 cells)	
C101	Whole cell size	122 ± 31	117 ± 38	μm^2
C102	The sum of mother and daughter cell outline length	15.8 ± 3.4	15.7 ± 3.9	μm
C103	Long axis length in mother cell	0.577 ± 0.042	0.542 ± 0.061	μm
C104	Short axis length in mother cell	3.69 ± 0.37	3.49 ± 0.36	μm
C105	Neck position	3.79 ± 0.74	4.64 ± 2.98	radian
C106	Bud direction	5.54 ± 1.38	5.92 ± 3.65	radian
C107	Long axis length in bud	2.44 ± 0.85	2.67 ± 0.77	μm
C108	Short axis length in bud	19.8 ± 3.8	21.9 ± 5.5	μm
C109	Neck width	12.0 ± 0.7	12.2 ± 1.9	μm
C110	Distance between bud tip and mother long axis extension	2.71 ± 0.79	2.63 ± 1.16	μm
C111	Distance between bud tip and mother short axis extension	3.56 ± 0.71	3.25 ± 1.74	μm
C112	Distance between middle point of neck and mother center	2.12 ± 0.28	1.91 ± 0.19	μm

C113	Distance between bud tip and mother long axis through middle point of neck	31.2 ± 6.0	30.6 ± 3.6	μm
C114	Bud axis ratio	0.930 ± 0.174	0.942 ± 0.115	
C115	Mother axis ratio	1.21 ± 0.07	1.20 ± 0.11	
C116	Axis ratio ratio	0.767 ± 0.146	0.786 ± 0.117	
C117	Cell outline ratio	0.556 ± 0.195	0.681 ± 0.208	
C118	Cell size ratio	0.386 ± 0.218	0.515 ± 0.251	
C128	Distance between middle point of neck and mother hip	4.20 ± 0.49	3.88 ± 0.38	μm

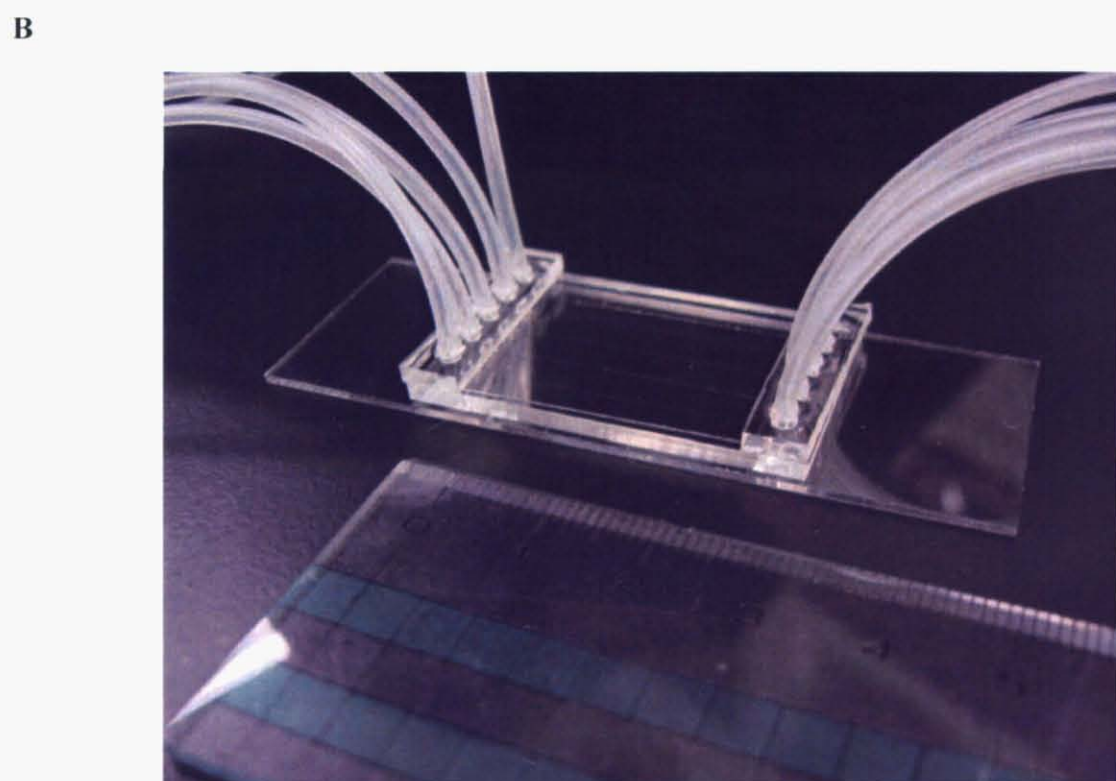
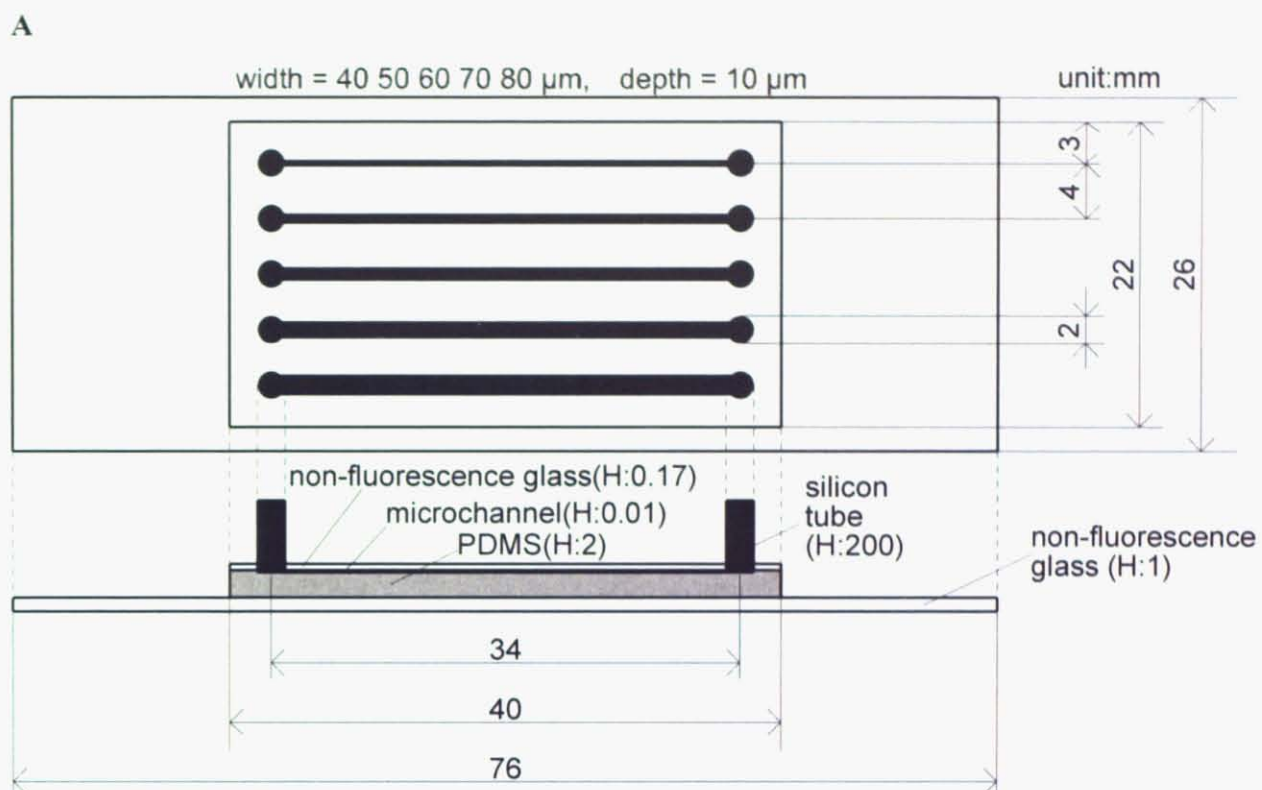
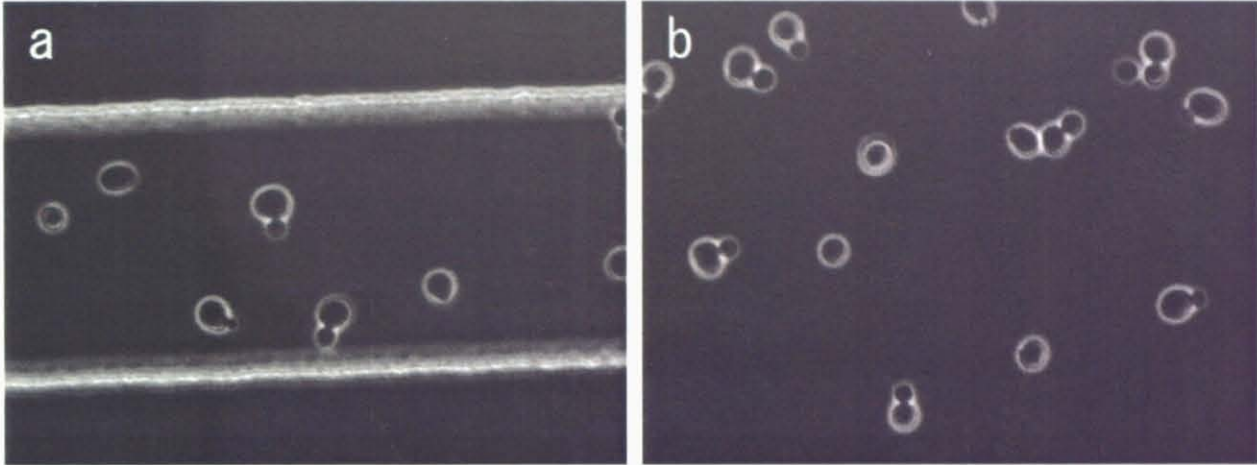


Figure 10.

A



B

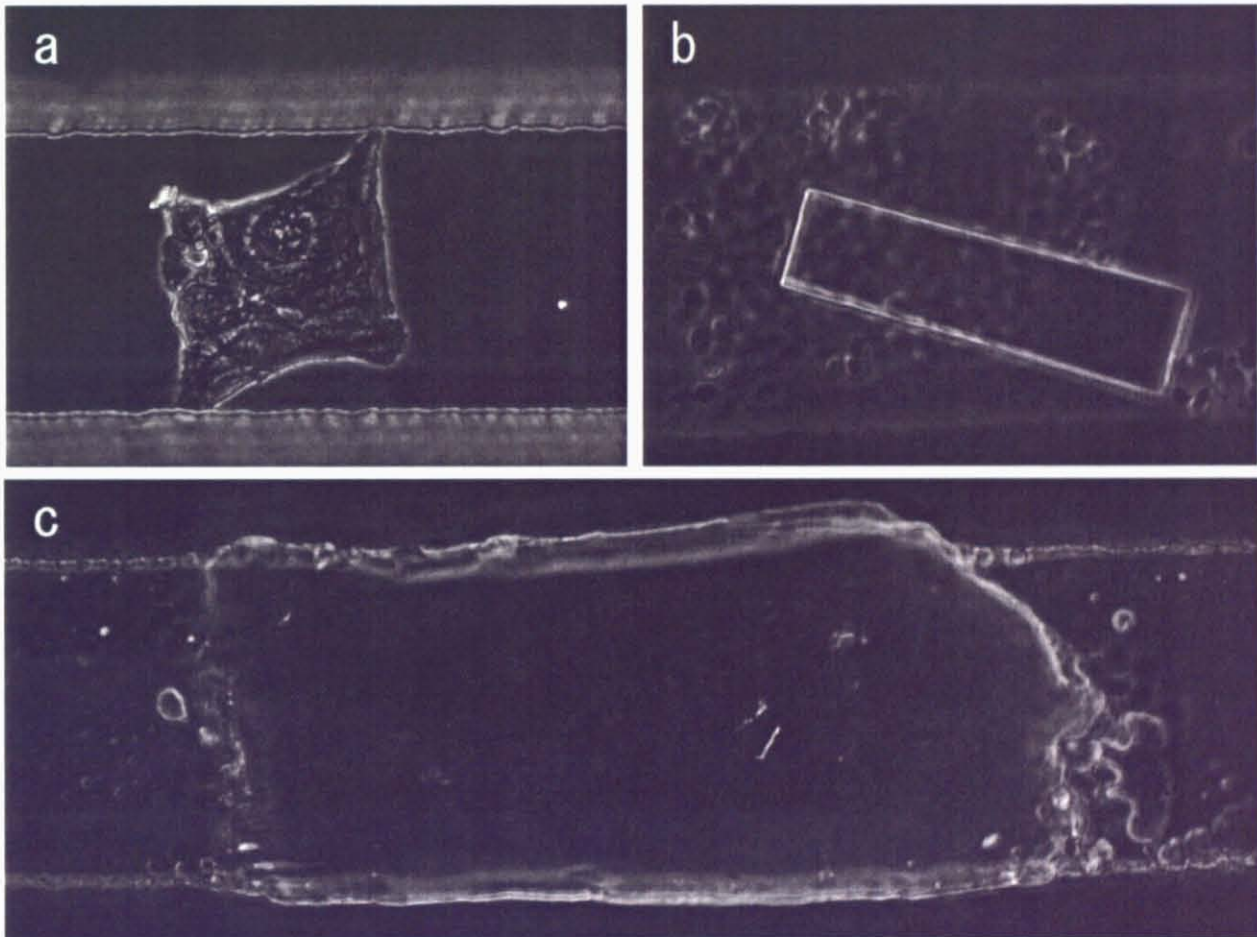
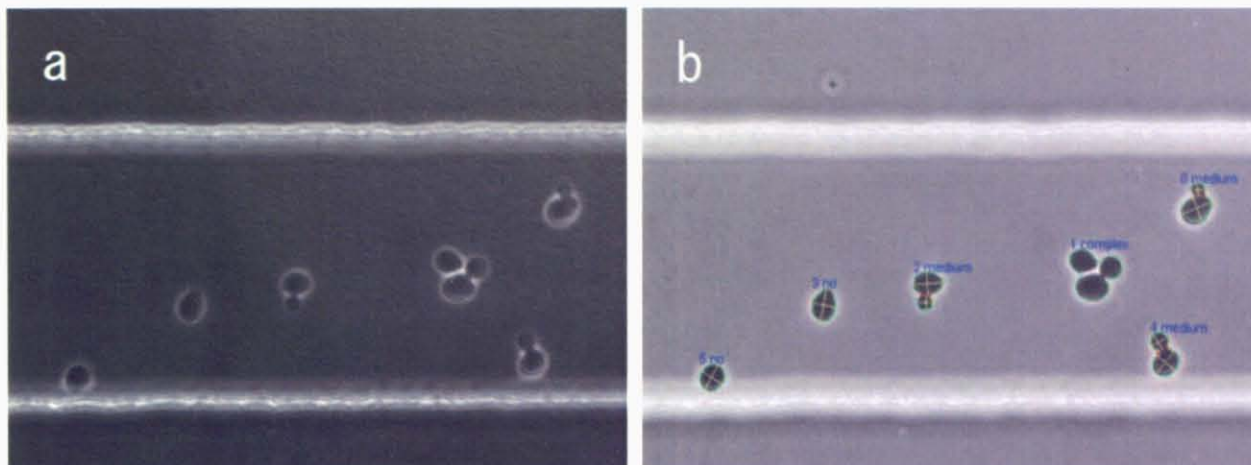


Figure 11.

A



B

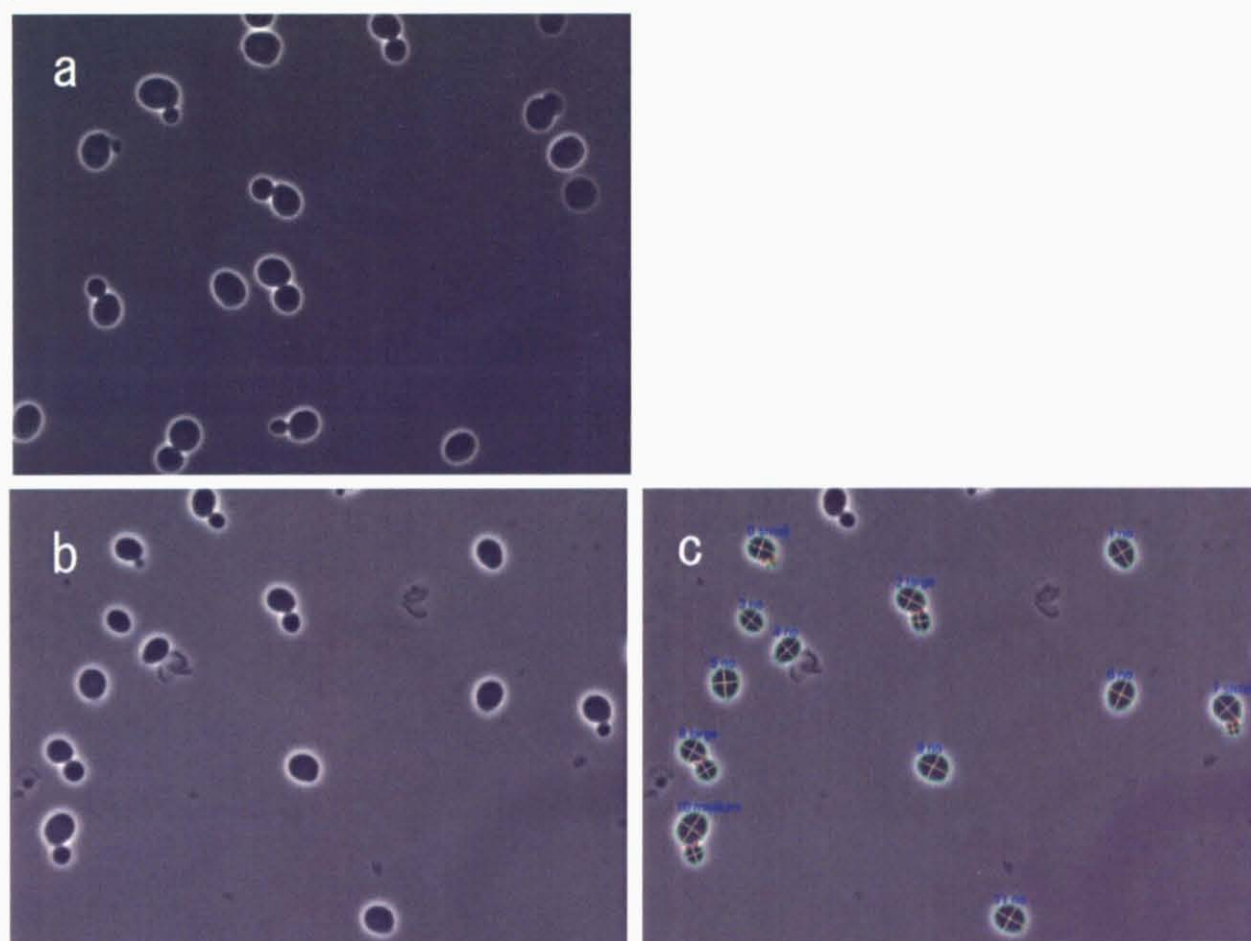


Figure 12.

REFERENCES

- Allison, D. B., Cui, X., Page, G. P., and Sabripour, M. (2006). Microarray data analysis: from disarray to consolidation and consensus. *Nat Rev Genet* 7, 55-65.
- Balagadde, F. K., You, L. C., Hansen, C. L., Arnold, F. H., and Quake, S. R. (2005). Long-term monitoring of bacteria undergoing programmed population control in a microchemostat. *Science* 309, 137-140.
- Bi, E., and Pringle, J. R. (1996). *ZDS1* and *ZDS2*, genes whose products may regulate Cdc42p in *Saccharomyces cerevisiae*. *Mol Cell Biol* 16, 5264-5275.
- Brown, J. A., Sherlock, G., Myers, C. L., Burrows, N. M., Deng, C., Wu, H. I., McCann, K. E., Troyanskaya, O. G., and Brown, J. M. (2006). Global analysis of gene function in yeast by quantitative phenotypic profiling. *Mol Syst Biol* 2, 2006 0001.
- Churchill, G. A., and Doerge, R. W. (1994). Empirical threshold values for quantitative trait mapping. *Genetics* 138, 963-971.
- Cunningham, K. W., and Fink, G. R. (1994). Calcineurin-dependent growth control in *Saccharomyces cerevisiae* mutants lacking *PMCI*, a homolog of plasma membrane Ca^{2+} ATPases. *J Cell Biol* 124, 351-363.
- Eisen, M. B., Spellman, P. T., Brown, P. O., and Botstein, D. (1998). Cluster analysis and display of genome-wide expression patterns. *Proc Natl Acad Sci U S A* 95, 14863-14868.
- El-Ali, J., Sorger, P. K., and Jensen, K. F. (2006). Cells on chips. *Nature* 442, 403-411.
- Fujii, T., Sando, Y., Higashino, K., and Fujii, Y. (2003). A plug and play microfluidic device. *Lab on*

a Chip 3, 193-197.

Fukuoka, D. (2004). Novel method for systematic analysis of essential genes in *Saccharomyces cerevisiae*. Master thesis.

Garge, N. R., Page, G. P., Sprague, A. P., Gorman, B. S., and Allison, D. B. (2005). Reproducible clusters from microarray research: whither? BMC Bioinformatics 6 Suppl 2, S10.

Hartwell, L. H. (1991). Twenty-five years of cell cycle genetics. Genetics 129, 975-980.

Hirata, R., Umemoto, N., Ho, M. N., Ohya, Y., Stevens, T. H., and Anraku, Y. (1993). *VMA12* is essential for assembly of the vacuolar H⁺-ATPase subunits onto the vacuolar membrane in *Saccharomyces cerevisiae*. J Biol Chem 268, 961-967.

Kohane, I. S., Kho, A. T., and Butte, A. J. (2003). Microarrays for an integrative genomics (Cambridge, Mass: MIT Press).

Kucharczyk, R., Kierzek, A. M., Slonimski, P. P., and Rytka, J. (2001). The Ccz1 protein interacts with Ypt7 GTPase during fusion of multiple transport intermediates with the vacuole in *S. cerevisiae*. J Cell Sci 114, 3137-3145.

Kwok, E. Y., Severance, S., and Kosman, D. J. (2006). Evidence for iron channeling in the Fet3p-Ftr1p high-affinity iron uptake complex in the yeast plasma membrane. Biochemistry 45, 6317-6327.

Lord, P. G., and Wheals, A. E. (1983). Rate of cell cycle initiation of yeast cells when cell size is not a rate-determining factor. J Cell Sci 59, 183-201.

Lynn, R. R., and Magee, P. T. (1970). Development of the spore wall during ascospore formation in

Saccharomyces cerevisiae. J Cell Biol 44, 688-692.

Mann, H. B., and Whitney, D. R. (1947). On a Test of Whether One of 2 Random Variables Is Stochastically Larger Than the Other. Annals of Mathematical Statistics 18, 50-60.

Manz, A., Harrison, D. J., Verpoorte, E. M. J., Fettingner, J. C., Paulus, A., Ludi, H., and Widmer, H. M. (1992). Planar Chips Technology for Miniaturization and Integration of Separation Techniques into Monitoring Systems - Capillary Electrophoresis on a Chip. Journal of Chromatography 593, 253-258.

Mizunuma, M., Hirata, D., Miyahara, K., Tsuchiya, E., and Miyakawa, T. (1998). Role of calcineurin and Mpk1 in regulating the onset of mitosis in budding yeast. Nature 392, 303-306.

Mizunuma, M., Miyamura, K., Hirata, D., Yokoyama, H., and Miyakawa, T. (2004). Involvement of S-adenosylmethionine in G1 cell-cycle regulation in *Saccharomyces cerevisiae*. Proc Natl Acad Sci U S A 101, 6086-6091.

Mosch, H. U., and Fink, G. R. (1997). Dissection of filamentous growth by transposon mutagenesis in *Saccharomyces cerevisiae*. Genetics 145, 671-684.

Ng, J. M. K., Gitlin, I., Stroock, A. D., and Whitesides, G. M. (2002). Components for integrated poly(dimethylsiloxane) microfluidic systems. Electrophoresis 23, 3461-3473.

Ohtani, M., Saka, A., Sano, F., Ohya, Y., and Morishita, S. (2004). Development of image processing program for yeast cell morphology. J Bioinform Comput Biol 1, 695-709.

Ohya, Y., Miyamoto, S., Ohsumi, Y., and Anraku, Y. (1986a). Calcium-sensitive *cls4* mutant of *Saccharomyces cerevisiae* with a defect in bud formation. J Bacteriol 165, 28-33.

- Ohya, Y., Ohsumi, Y., and Anraku, Y. (1986b). Isolation and characterization of Ca^{2+} -sensitive mutants of *Saccharomyces cerevisiae*. *J Gen Microbiol* 132, 979-988.
- Ohya, Y., Sese, J., Yukawa, M., Sano, F., Nakatani, Y., Saito, T. L., Saka, A., Fukuda, T., Ishihara, S., Oka, S., *et al.* (2005). High-dimensional and large-scale phenotyping of yeast mutants. *Proc Natl Acad Sci U S A* 102, 19015-19020.
- Ohya, Y., Umemoto, N., Tanida, I., Ohta, A., Iida, H., and Anraku, Y. (1991). Calcium-sensitive *cls* mutants of *Saccharomyces cerevisiae* showing a Pet^- phenotype are ascribable to defects of vacuolar membrane H^+ -ATPase activity. *J Biol Chem* 266, 13971-13977.
- Pruyne, D., and Bretscher, A. (2000). Polarization of cell growth in yeast. I. Establishment and maintenance of polarity states. *J Cell Sci* 113 (Pt 3), 365-375.
- Rieder, S. E., and Emr, S. D. (1997). A novel RING finger protein complex essential for a late step in protein transport to the yeast vacuole. *Mol Biol Cell* 8, 2307-2327.
- Schmitt, J. M., and Kumar, G. (1996). Turbulent nature of refractive-index variations in biological tissue. *Opt Lett* 21, 1310.
- Suzuki, R., and Shimodaira, H. (2006). Pvcust: an R package for assessing the uncertainty in hierarchical clustering. *Bioinformatics* 22, 1540-1542.
- Takita, Y., Ohya, Y., and Anraku, Y. (1995). The *CLS2* gene encodes a protein with multiple membrane-spanning domains that is important Ca^{2+} tolerance in yeast. *Mol Gen Genet* 246, 269-281.
- Trueheart, J., Boeke, J. D., and Fink, G. R. (1987). Two genes required for cell fusion during yeast

conjugation: evidence for a pheromone-induced surface protein. *Mol Cell Biol* 7, 2316-2328.

Unger, M. A., Chou, H. P., Thorsen, T., Scherer, A., and Quake, S. R. (2000). Monolithic microfabricated valves and pumps by multilayer soft lithography. *Science* 288, 113-116.

Whitesides, G. M. (2006). The origins and the future of microfluidics. *Nature* 442, 368-373.

Yokoyama, H., Mizunuma, M., Okamoto, M., Yamamoto, J., Hirata, D., and Miyakawa, T. (2006).

Involvement of calcineurin-dependent degradation of Yap1p in Ca^{2+} -induced G_2 cell-cycle regulation in *Saccharomyces cerevisiae*. *EMBO Rep* 7, 519-524.

Yoshimoto, H., Saltsman, K., Gasch, A. P., Li, H. X., Ogawa, N., Botstein, D., Brown, P. O., and Cyert, M. S. (2002). Genome-wide analysis of gene expression regulated by the calcineurin/Crz1p signaling pathway in *Saccharomyces cerevisiae*. *J Biol Chem* 277, 31079-31088.

Yu, Y., Jiang, Y. W., Wellinger, R. J., Carlson, K., Roberts, J. M., and Stillman, D. J. (1996). Mutations in the homologous *ZDS1* and *ZDS2* genes affect cell cycle progression. *Mol Cell Biol* 16, 5254-5263.

Zhang, J. W., Parra, K. J., Liu, J., and Kane, P. M. (1998). Characterization of a temperature-sensitive yeast vacuolar ATPase mutant with defects in actin distribution and bud morphology. *J Biol Chem* 273, 18470-18480.

PUBRICATIONS

Peer reviewed Paper

“Diversity of Ca^{2+} -induced morphology revealed by morphological phenotyping of Ca^{2+} -sensitive mutants of *Saccharomyces cerevisiae*”

Shinsuke Ohnuki, Satoru Nogami, Hanako Kanai, Dai Hirata, Yoichiro Nakatani, Shinichi

Morishita and Yoshikazu Ohya

Eukaryotic Cell, in press

Presentation in Scientific Meeting

“Quantitative morphological analyses of calcium-sensitive mutants of *Saccharomyces cerevisiae*”

Shinsuke Ohnuki, Satoru Nogami, Dai Hirata, Yoichiro Nakatani, Shinichi Morishita, Yoshikazu

Ohya

20th IUBMB International Congress of Biochemistry and Molecular Biology and 11th FAOBMB

Congress

June 23, 2006, Kyoto, poster

“Analysis of Ca^{2+} induced morphological change in *Saccharomyces cerevisiae*”

Shinsuke Ohnuki, Mizuho Sekiya, Satoru Nogami, Yoichiro Nakatani, Shinichi Morishita,

Yoshikazu Ohya

28th Annual Meeting of the Molecular Biology Society of Japan

December 9, 2005, Fukuoka, poster (domestic)